SUBMISSION TO CANADIAN GEOTECHNICAL JOURNAL

DATE:

02/05/2019

TITLE:

Shallow penetrometer tests – Theoretical and experimental modelling of penetration and dissipation stages

AUTHOR:

Schneider, M.A.[1], Stanier, S.A.[2], White, D.J.[3] and Randolph, M.F.[4]

POSITION AND AFFILIATION:

[1] Research Student at the Centre for Offshore Foundation Systems, University of Western Australia

[2] University Senior Lecturer, Cambridge University Engineering Department, Trumpington Street, Cambridge, CB2 1PZ.

[3] Professor, University of Southampton (also affiliated to the University of Western Australia)

[4] Professor at the Centre for Offshore Foundation Systems, University of Western Australia

CONTACT ADDRESS:

Dr Sam Stanier
Cambridge University Engineering Department
Trumpington Street
Cambridge
CB2 1PZ
United Kingdom
Email: sas229@cam.ac.uk

NUMBER OF WORDS, FIGURES AND TABLES:

Words: 5892
Figures: 13
Tables: 5

KEYWORDS:

Shallow penetrometer; offshore engineering; in-situ testing; undrained penetration; dissipation

SHALLOW PENETROMETER TESTS – THEORETICAL AND EXPERIMENTAL MODELLING OF PENETRATION AND DISSIPATION STAGES

Schneider, M.A., Stanier, S.A., White, D.J. and Randolph, M.F.

ABSTRACT

Shallow penetrometers are devices that penetrate into and measure the properties of surficial offshore sediments via multi-phase tests involving penetration, dissipation and rotation stages. In fine grained soils such as silts and clays, these testing stages yield undrained strength, consolidation and friction properties relevant to subsea pipeline and shallow foundation design. This paper describes toroid and hemiball devices of the scale for use in box core samples, and associated interpretation methods for the penetration and dissipation stages. The aim of the paper is to provide all tools needed to design and interpret these tests. New large deformation finite element (LDFE) dissipation solutions are presented, which can be used for back-analysis of the dissipation stage. Results of an extensive laboratory proof testing exercise in kaolin clay, for both the hemiball and toroid penetrometer, are also reported. These results highlight the potential of the two devices to quickly and economically assess strength and consolidation characteristics of fine-grained sediments in box-core samples recovered to the deck of a site investigation vessel.

INTRODUCTION

Many offshore structures – such as pipelines and shallow foundations – rest on soft surficial marine clays. Reliable characterisation of these top soil layers (often only half a metre) is key to developing robust and cost-effective designs for such infrastructure.

Conventional in-situ testing procedures (e.g. CPT, T-bar or ball penetrometers) may be used to assess the shear strength profile of surficial soils (e.g. White et al. (2010a) for the T-bar or Morton et al. (2014) for the ball penetrometer), although only very limited information about the interface friction properties can be gained with such testing methods. Recovering tube samples for laboratory testing (e.g. in-situ coring of the seabed or recovering tube samples from a box-core sample on the deck of a survey vessel) is difficult, mainly because of sampling-induced disturbance of such soft materials, which adversely affects element test results (Baligh et al., 1987; Clayton et al., 1998; Hover et al., 2013; Pineda et al. 2016). Additionally, element tests, in particular the interface shear box test (Westgate et al., 2018), should be representative of the conditions encountered offshore. At the low effective normal stress levels (σ'_n ~10 kPa) relevant to subsea pipelines and shallow foundations, it is challenging to perform and interpret element tests due to spurious system friction generated by the apparatus. Corrections for these errors (e.g. Lehane & Liu, 2013) become an increasingly large proportion of the measured overall system response as the effective normal stress levels reduce. The Cam-Tor apparatus (Kuo et al., 2015) and the tilt table (Pedersen et al., 2003) are two alternative testing techniques better suited to making measurements of drained interface friction at low stress levels. However, the sample recovery and transportation process, from an offshore testing site to an onshore laboratory, leads to significant time delays and the risk of sample disturbance.

The toroid and hemiball penetrometer, two novel pipe-like investigation devices, have the potential to address these limitations (Yan et al., 2011a; Stanier & White, 2014). They are capable of measuring near-surface soil properties in-situ offshore at the seabed (deployed from either a frame or remotely operated vehicle (ROV)) or in a recovered box-core (generally 0.5

m by 0.5 m in plan) on the deck of a survey vessel. A shallow penetrometer test is typically subdivided into penetration, dissipation and rotation stages, targeting respectively the strength, consolidation and interface friction characteristics of the underlying soil.

A major advantage of the shallow penetrometers is that the rotation stage of the tests may be interpreted using an effective stress approach, as pore water pressures are continuously monitored via pressure transducers at various locations on the devices. In addition there are two key advantages to the shallow penetrometer concept compared to the current 'gold standard', which is in-situ model testing performed using systems such as the Fugro SMARTPIPE (White et al., 2010b), namely that: (i) continuous rotation effectively facilitates infinite sliding without the end effects associated with testing using an instrumented section of pipeline; and (ii) the modest penetrometer diameters of box-core sized devices (25 to 100 mm) result in relatively short test durations which allows the devices to be used 'off the critical path' of operations during a geophysical or geotechnical survey.

The concept of the shallow penetrometer devices was first explored by Yan et al. (2011a, 2011b) via small scale centrifuge tests and small strain finite element (SSFE) simulations. Stanier & White (2014) investigated the initial undrained penetration stage in more detail and eventually developed an interpretation model, based on a series of comprehensive large deformation finite element analysis (LDFE). Following these initial studies, 'box-core scale' versions of the penetrometers and a bespoke actuation system were manufactured at the University of Western Australia (see Figure 1) as part of the Remote Intelligent Geotechnical Seabed Surveys Joint Industry Project (RIGSS JIP). Schneider et al. (2019a) provide a comprehensive description of the design of these 'box core scale' devices and associated system design considerations.

This paper and the accompanying companion paper (Schneider et al., 2019b) describe new interpretation methodologies for these 'box-core scale' penetrometers and validate their operation in laboratory conditions. This paper illustrates the fundamentals of the penetration

and dissipation phase, while the rotation stage is outlined in the companion paper. The 'box core scale' hemiball has pore pressure sensors at the mid-face (45° from the invert) and so-called intermediate (22.5° from the invert) locations as illustrated in Figure 2. New hemiball LDFE-dissipation solutions have been developed that can be used to interpret pore pressure measurements taken at any location on the surface of the device, allowing flexibility in the design of future versions of the device. A comprehensive laboratory testing program, for both the hemiball and the toroid penetrometer (more detailed information about these devices can be found in the next section), was conducted in kaolin clay samples. The test results demonstrate the potential of the shallow penetrometers to rapidly and consistently measure the strength and consolidation characteristics of the soft fine-grained sediments prevalent on the ocean floor in deep water locations.

SHALLOW PENETROMETERS

Hemiball & toroid penetrometer

Both penetrometers feature a curved underside that represents the shape of pipe-like infrastructure (e.g. seabed cables or pipelines), consequently minimising uncertainties due to scaling for geometric effects (i.e. from planar interface properties measured in interface shear box tests to resistance on a curved pipeline). The device diameter, D, of the box-core sized penetrometers (Figure 1) was selected as 100 mm and 25 mm for the hemiball and toroid, respectively. For the toroid (Figure 2) an aspect ratio of $L/D = 2$, where L is the lever arm of the toroidal cylinder, was chosen to minimise adverse effects due to interference across the device after Yan et al. (2011a).

Both penetrometers feature pressure transducers (PPT) at various locations on the device interface, as illustrated in Figure 2. Four transducers are installed at the tip of the toroid, referred to here as the invert position (abbr. *inv*). The hemiball features 5 pressure transducers, with two sensors at the intermediate (abbr. *int*; $\theta = 22.5°$) and midface (abbr. *mf*; $\theta = 45°$) locations and

one at the device tip. The pore pressure sensors allow the dissipation characteristics of the soil to be measured and facilitate effective stress interpretations of the rotation stage. For larger penetrometers, intended for direct in-situ deployment via a seabed frame or ROV, additional pore pressure sensors could be added at different locations on the device surface. Schneider et al. (2019a) describe in more details the penetrometers and the actuator developed to operate them.

Envisaged testing stages

A single test is sufficient to deduce the key soil parameters required for contemporary pipeline design (DNV-RP-F110, 2007). The tests are relatively brief and thus suitable for in-situ box-core testing on a site investigation vessel, during either a geophysical or geotechnical site survey. Table 1 shows the envisaged testing stages alongside the soil properties that can be estimated in each phase. The strength (s_u) and dissipation characteristics (c_v) are evaluated in the penetration and consolidation stage, respectively. The rotation stage and variations of it are used to evaluate the frictional penetrometer-soil interaction properties (τ_u , δ). Friction characteristics of the sediment ($s_{u,int}$, ϕ') can be directly assessed using a device with a completely rough interface (average surface roughness, R_a > 100 μm; Meyer et al., 2015). Once all excess pore water pressures have dissipated after a sufficiently long rotation phase, the device can be subjected to additional penetration in order to generate a measure of the consolidated undrained shear strength ($s_{u,c}$).

Table 1: Targeted soil properties of shallow penetrometer testing stages.

Main testing phases		Relevant measure	Properties of interest
1	Penetration	V, w	s_u , ($s_{u,rem}$)
2	Consolidation	u	c_v
3	Rotation	T, u, w	τ_u , δ, ϕ', (κ/λ) *
4	(Extra penetration)	V, w	($s_{u,c}$)

* Different properties can be evaluated based on rotation rate, device actuation and roughness.

Note: the measures V, w, u and T represent the measured vertical load, the recorded probe embedment, the pore water pressures and the mobilised torque, respectively. The remoulded shear strength and the elastic-plastic volumetric stiffness ratio are denoted by $s_{u,rem}$ and κ/λ.

INTERPRETATION OF PENETRATION & DISSIPATION STAGES

Undrained penetration

As for pipelines, undrained conditions apply for penetration at dimensionless velocities, V_{pen}, greater or equal to ~100 (Chatterjee et al., 2013). The dimensionless velocity is expressed as a function of the penetration speed, v_{pen}, the device diameter, D, and the coefficient of consolidation, c_v, as:

$$V_{pen} = \frac{v_{pen} D}{c_v} \geq 100 \tag{1}$$

When planning a shallow penetrometer test routine, the following considerations regarding the target penetration depth, w, need to be taken into account:

1. Select w/D so that effective normal stresses on the interface of the device are within the range of practical interest (after dissipation), which is typically ~5-20 kPa for subsea pipelines (e.g. push device to w/D = 0.3 and unload to project-relevant stress level if excessive resistance is experienced).

2. Target $0.15 \leq w/D \leq 0.5$ so that the geometric similarity between the shallow penetrometer and subsea pipelines is achieved (e.g. initial penetration to $w/D = 0.3$ would provide some allowance for additional settlement during the dissipation and rotation stage, whilst keeping $w/D \leq 0.5$).
3. For the hemiball, ensure $w/D \geq \sim 0.15$ so that the midface pressure transducers are fully embedded in soil at the end of the penetration stage.

For interpretation of the penetration stage, the linear model of Stanier & White (2014), which was developed from an extensive LDFE-study of shallow penetrometer penetration in fine-grained sediments for undrained conditions, is used to convert the measured vertical load to a linearly varying undrained shear strength profile. The total vertical penetrometer resistance, V, consists of two components: the geotechnical soil resistance, V_{geot}, and the soil buoyancy, V_b, which are defined as:

$$V = V_{geot} + V_b = N_{c,nom}\, A_{nom}\, s_{u0} + f_b V_s \gamma' \tag{2}$$

In the geotechnical resistance term $N_{c,nom}$ is a bearing capacity factor, A_{nom} the nominal bearing area ($\pi D^2/4$ and $2\pi LD$ for the hemiball and toroid, respectively) and s_{u0} the undrained shear strength at the current depth of the invert of the device. In the soil buoyancy term f_b is an enhancement factor that accounts for the relative increase in resistance beyond Archimedes' principle that is caused by local soil heave around the periphery of the device, V_s is the volume of soil displaced by the penetration of the device (embedded volume relative to original mudline) and γ' the effective unit weight of the soil.

The model is used to evaluate the mudline strength, $s_{u,m}$, as well as the strength gradient k_{su} by performing iterations until the measured and theoretical profiles align. The bearing capacity factor, $N_{c,nom}$, is estimated iteratively as a function of the normalised embedment, w/D, and the strength parameter $s_{u,avg}$, which is the average shear strength between the mudline and a depth

of one penetrometer diameter (i.e. $s_{u,avg} = s_{u,m} + 0.5k_{su}D$). Figure 3 demonstrates this back-analysis method for a toroid test, eventually leading to an excellent match between test measurements and the analytical model. More information regarding the procedure is found in Stanier & White (2014).

Cyclic penetration (CRT)

The cyclic remoulding test (CRT) is a variation of the monotonic penetration test where the device is cyclically penetrated into and out of the soil at an undrained penetration rate ($V_{pen} \geq 100$) in an attempt to mimic the effects of pipe laying processes (10 penetration-extraction cycles with an amplitude of $0.15D$ were modelled in this study). In addition to the initial undrained strength profile of the soil, a measure of the remoulded strength, $s_{u,rem}$, and the soil sensitivity, S_t, may be derived. Examples of this variant of penetration test are presented later in the manuscript.

Consolidation stage

For the consolidation stage, the vertical load recorded at the final penetration depth is held constant (load-controlled mode: $V=V_{max}$) in order to mimic the self-weight of a pipe-like structure. The coefficient of consolidation can be estimated reliably if the dissipation process is monitored until at least 50% of the initial excess pore pressures have dissipated (i.e. final drainage index $\psi > 0.5$, with $\psi = 1-\Delta u/\Delta u_{ini}$). This provides a sufficient proportion of the dissipation response to allow accurate fitting to the theoretical solution, using the same approach as is common for cone penetrometer dissipation tests. However, if the undrained interface strength of the seabed is to be determined after full consolidation under the weight of a pipe or foundation in the subsequent rotation stage, it is better to allow > 90% of the initial excess pore pressures to dissipate (i.e. where the final drainage index $\psi > 0.9$). The general dissipation response of soil can be fitted with a hyperbolic function in terms of the normalised excess pore pressure as follows:

$$\frac{\Delta u}{\Delta u_{ini}} = \frac{1}{1+\left(T_{dis}/T_{dis,50}\right)^{m}} \qquad with \qquad T_{dis} = \frac{c_v\, t_{dis}}{D^2} \tag{3}$$

The dimensionless time, T_{dis}, is a function of the consolidation coefficient, c_v, the dimensional dissipation time, t_{dis}, and the penetrometer diameter, D. The shape of the hyperbolic relationship is governed by the parameters m and $T_{dis,50}$ (dimensionless time at which ~50% of consolidation has finished), which are fitting parameters derived from numerical simulations. Rearrangement of Equation (3) leads to the following expression

$$t_{dis} = \frac{D^2\, T_{dis,50}}{c_v}\left(\frac{\psi}{1-\psi}\right)^{1/m} \tag{4}$$

which can be used to estimate the timescales of shallow penetrometer dissipation tests for particular values of the coefficient of consolidation, c_v.

The fitting parameters in Equation (3) and (4) can be defined in terms of the dissipation response at a specific transducer location on the device interface ($T_{dis,50}$ and m) or the average pore pressure dissipation on the embedded penetrometer surface ($T_{dis,50,ave}$ and m_{ave}). The parameters associated with a specific spot measurement (here: invert location) are of practical relevance for determining the coefficient of consolidation of soil, whereas the parameters characterising the periphery dissipation response can be used to estimate timescales (e.g. for the increase in friction around the device due to the drainage of excess pore pressures).

Yan et al. (2017) published SSFE-solutions for both the 'invert' and 'average' values, which can be used in conjunction with Equation (3) or (4). The hemiball and toroid solutions given are based on wished-in-place simulations (in other words the soil that would have occupied the final position of the penetrometer (including shaft) is simply replaced by the penetrometer) developed using the Modified Cam Clay soil model, hence ignoring the influence of penetration-induced soil heave around the penetrometer.

LDFE-modelling techniques provide more realistic results, as the propensity for soil heave and other influences of the penetration process are captured. Yan et al. (2011a) showed that a toroid with an aspect ratio, L/D, of 2 or higher suffers from minimal to no interference across the device, meaning that pipeline solutions can be adopted with sufficient accuracy (e.g. LDFE-pipeline solutions after Chatterjee et al. (2012), as specified in Table 2). No LDFE-dissipation solutions for a rough hemiball have been published to date. To address this gap, LDFE-simulations modelling the process of excess pore pressure dissipation around a rough hemiball were conducted, as presented in the next section.

Table 2: Hyperbolic fits of dissipation response at penetrometer invert (normally consolidated soils).

w/D	***LDFE – Solutions***			
	Toroid (rough) [#]		Hemiball (rough)	
	$T_{dis,50}$	*m*	$T_{dis,50}$	*m*
0.1	0.028	1.05	*This study (see also Table 4)*	
0.2	0.055	1.05		
0.3	0.075	1.05		
0.4	0.110	1.05		
0.5	0.135	1.05		

[#] Values after Chatterjee et al. (2012), assuming that a toroid is equivalent to a pipe for $L/D \geq 2$

An example application of Equation (3) using the coefficients in Table 2 is given in Illustration of back-analysis procedure after Stanier & White (2014) for a toroid test: (a) bearing capacity factor model fit; and (b) the derived undrained strength profile.

Figure 4 for a toroid test performed on kaolin clay. Illustration of back-analysis procedure after Stanier & White (2014) for a toroid test: (a) bearing capacity factor model fit; and (b) the derived undrained strength profile.

Figure 4a shows raw dissipation measurements for all four pore pressure transducers (PPTs), which are at equidistant circumferential locations around the toroid at the penetrometer invert. The measured average excess pore pressure is then corrected for measurement lag according to the procedure proposed by Sully et al. (1999), as illustrated in Illustration of back-analysis procedure after Stanier & White (2014) for a toroid test: (a) bearing capacity factor model fit; and (b) the derived undrained strength profile.

Figure 4b. The initial excess pore pressure value, Δu_{ini}, is derived via back-extrapolation of the (averaged) test measurements in root-time space. The coefficient of consolidation corresponding to the depth of the penetrometer invert, c_{v0}, can then be estimated by fitting the normalised dissipation response to a theoretically derived FE-solution (e.g. Table 2) at $\Delta u/\Delta u_{ini}$ ~0.5 for the current embedment (with model coefficients interpolated from the listed values, if necessary), as illustrated in Illustration of back-analysis procedure after Stanier & White (2014) for a toroid test: (a) bearing capacity factor model fit; and (b) the derived undrained strength profile.

Figure 4c.

NEW DISSIPATION SOLUTIONS FOR HEMIBALL (LDFE)

The following solutions were generated using the Remeshing and Interpolation Technique with Small Strains (RITSS) methodology after Hu & Randolph (1998), which was implemented in the FE-software package ABAQUS (Dassault Systemes, 2011), using a combination of Python and FORTRAN-scripts, similar to the approach described in Wang et al. (2010). The large deformation modelling procedure simulates the undrained penetration stage as a series of consecutive small increments in order to avoid significant mesh distortions. After every calculation step the model domain is remeshed and all stress and state parameters are transferred to the new mesh for the next step, adopting the super-convergent patch recovery method after

Zienkiewicz & Zhu (1992) and finite element shape functions based interpolation techniques. The same procedure was used to define the initial conditions of the dissipation phase (geometry, stress and state parameters at the end of the LDFE penetration stage transferred to a new mesh), which was then modelled as a single small strain simulation.

Table 3: Used Modified Cam Clay parameters (Stewart, 1992)

Assumed soil parameters	**Value**
Critical state constant, M	0.92
Void ratio on CSL (at p' = 1 kPa), e_{cs}	2.14
Slope of normal consolidation line, λ	0.205
Slope of swelling line, κ	0.044
Poisson's ratio, υ	0.30
Soil permeability, k (m/s)	$1 \cdot 10^{-9}$
Effective unit weight, γ' (kN/m^3)	5.0
Over-consolidation ratio, OCR	1.0
Unit weight of water, γ_w (kN/m^3)	10

The shallow penetrometer and soil were modelled using axial symmetry with free distances to the domain boundaries that were sufficiently large to minimise boundary effects (radius: ~8D; depth: ~10D). To capture the penetration-induced pore pressure generation and dissipation in normally consolidated soil representative of deep water sediments, the Modified Cam Clay soil model of Roscoe & Burland (1968) was used in conjunction with the soil parameters listed in Table 3. The earth pressure coefficient, K_0, was estimated empirically as 1-sinϕ'_{cv} (K_0 ~0.6). Selection of reduced integration quadrilateral coupled pore pressure elements (type: CAX8RP) and enforcement of a minimum applicable time increment (Vermeer & Verruijt, 1981; Dassault Systemes, 2011) led to significantly shorter calculation times and improved solution stability compared to triangular elements. A mesh refinement algorithm was developed to control the maximum element size generated along the device interface during the periodic remeshing process. The mudline was specified as fully draining via a user-subroutine, by prescribing hydrostatic conditions (relative to the original intact mudline) to any surface boundary node

that was not in direct contact with the penetrometer. Drainage was precluded where the penetrometer was in contact with the soil. The 'rough' contact formulation was used to model the coarse surface texture of the current hemiball device. A small surcharge, q_0, of ~1 kPa (quasi-uniform conditions of s_u and c_v over depth range of interest, as $q_0/\gamma' D = 2$) was required to achieve convergence at the free-surface of the soil and to create a shear strength intercept at the mudline. The appropriateness of the adopted mesh density and penetration rate (V_{pen} ~100) was confirmed through sensitivity analyses (see also Schneider et al., 2018).

Undrained penetration resistance

Rearrangement of Equation (2) allows the normalised penetration resistance, $N_{c,nom}$, to be expressed as

$$N_{c,nom} = \left(\frac{V_{geot}}{A_{nom}\, s_{u0}} \right) = \left(\frac{V}{A_{nom}\, s_{u0}} \right) - f_b \left(\frac{\gamma' \cdot V_s}{A_{nom}\, s_{u0}} \right) \quad with \quad A_{nom} = \frac{\pi D^2}{4} \tag{5}$$

Figure 5 shows the numerically derived resistance for the initial undrained penetration phase, up to an embedment of 0.5D. Solutions published by Stanier & White (2014) were used to determine the buoyancy factor, f_b, as a function of embedment, and hence submerged penetrometer volume, V_s. The undrained shear strength, s_{u0}, at the normalised embedment of the penetrometer invert, w/D, was estimated according to Wood (1990), as a function of the MCC-parameters indicated in Table 3.

Chatterjee et al. (2014) reported results for the penetration of the 'parkable piezoprobe', which are comparable to the smooth hemiball calculations, as the geometry of the two devices is the same, thus validating the used FE-model (Figure 5). Large deformation Tresca analyses were published by Stanier & White (2014), for both a smooth and rough hemiball. The lower penetration resistance (roughly ~15-20%) exhibited in the Tresca simulations of Stanier & White (2014) may be attributed to (i) the difference in yield surface shape between the two

models (Tresca hexagon vs. circumscribing von Mises circle in the deviatoric plane giving a maximum deviation of ~15% under plane strain conditions) and (ii) an under-prediction of the failure load due to the Tresca-Mises hybrid criterion implemented in the Mohr-Coulomb/Tresca model in ABAQUS (Taiebat & Carter, 2008).

Minor drainage and local re-distribution of excess pore pressures is also unavoidable during the penetration stage (MCC simulations) and may further increase the differences between the two genera of simulations.

Dissipation solutions

The non-dimensional dissipation response is shown in Figure 6, for a normalised embedment, w/D, of 0.3 and all three transducer locations. Just as for the results in Table 2 the solutions were normalized using the value of c_{v0} (coefficient of consolidation at penetrometer invert) defined as

$$c_{v0} = \frac{k}{m_v \gamma_w} = \frac{k\,(1+e_0)\,p_0'}{\lambda \gamma_w} \tag{6}$$

The compressibility index m_v, can be expressed as a function of the stiffness parameter λ (the slope of normal consolidation line), the initial mean effective stress, p'_0, and the initial void ratio, e_0.

New dissipation solutions were created via curve-fitting of the numerical LDFE data, using the hyperbolic relationship given in Equation (3). Table 4 lists the $T_{dis,50}$ and m values determined for the invert, intermediate and midface positions at various normalised embedment depths. No values are specified in instances where the sensor location was too close to the mudline, which leads to an inconsistent dissipation response.

Table 4: Hyperbolic fits corresponding to new LDFE-dissipation solutions at different penetrometer locations

Rough Hemiball – LDFE dissipation solutions						
w/*D*	Invert sensor		Intermediate sensor		Midface sensor	
	$T_{dis,50}$	*m*	$T_{dis,50}$	*m*	$T_{dis,50}$	*m*
0.10	0.0105	1.50	-	-	-	-
0.20	0.0200	1.45	0.0160	1.20	-	-
0.30	0.0285	1.45	0.0235	1.15	0.0210	1.00
0.40	0.0320	1.35	0.0275	1.10	0.0295	1.20
0.50	0.0335	1.30	0.0305	1.10	0.0315	1.20

The dissipation responses for all three transducer locations defined in Table 4 are normalised by the same coefficient of consolidation, c_{v0}, representative of intact soil conditions at the penetrometer invert for each normalised embedment depth, *w*/*D*. Consequently, back-analyses of a hemiball test should yield similar c_{v0} values for the three pore pressure sensor locations if the model is robust, as will be demonstrated later in the paper.

Figure 6 shows that a significant Mandel-Cryer effect (Mandel, 1950; Cryer, 1963), which is revealed by the initial rise in excess pore pressure, is only observed at the invert position of the penetrometer, and not at the other two transducer locations (Mandel-Cryer effect, with the observed rise in excess pore pressure due to a local increase in total stress during the early stages of the dissipation process). The phenomenon occurred for all embedment ratios, *w*/*D*, as also found in other studies of shallow penetration of rough structures (e.g. Chatterjee et al., 2012). For the invert solution the hyperbolic model of Equation (3) was fitted to the simulation data for $\Delta u/\Delta u_{ini} \leq 0.9$, essentially ignoring the Mandel-Cryer effect.

EXPERIMENTAL TESTING PROGRAMME

Sample preparation and characterisation

Four soft kaolin clay samples were consolidated in large strongboxes (length: 1300 mm; width: 390 mm) under an effective stress of ~20 kPa, before unloading and swelling to equilibrium.

This stress history yields samples with undrained strength of 1-2 kPa, approximately constant over the depth range of the tests, which is broadly representative of the strength of soft surficial clay found offshore in deep water locations (e.g. Randolph et al., 2018).

T-bar tests (D_{Tbar} = 5 mm) were conducted in each of the samples prior to shallow penetrometer testing. Each test ensured undrained penetration, with a penetration rate of $V_{pen} = v_{pen} D_{Tbar}/c_v >$ 30 after Finnie & Randolph (1994), and included 10 penetration-extraction cycles to assess the soil sensitivity. All soil samples were found to be laterally homogeneous, as the recorded soil strength profiles were practically uniform within each strongbox. Likewise, the measurements were also consistent across all four strongboxes, thus allowing direct comparison of the results of different shallow penetrometer tests, independent of the exact testing location or the strongbox in which they were performed. Small soil specimens, recovered with the miniature core sampler, were also analysed at the end of each testing session to provide the moisture content and thus void ratio and effective unit weight of the samples.

Shallow penetrometer testing

Due to the larger diameter of the hemiball (D = 100 mm) only four penetrometer tests could be performed in each strongbox whilst ensuring minimal boundary or interaction effects. For the toroid (D = 25 mm), five tests were possible. The greater number of toroid tests was possible since the absolute embedment depths (and hence soil disturbance) were much lower, even though the normalised embedment may be the same for both penetrometers (e.g. w/D = 0.3). The volume of soil displaced by the hemiball is significantly larger than for the toroid, which results in spatially more expansive failure mechanisms.

Undrained penetration

An initial embedment at the end of the penetration stage of w/D = 0.3 was targeted. This provided some allowance for settlement during dissipation and rotation, whilst keeping $w/D \leq$

0.5. For the samples tested it also resulted in effective normal contact stresses on the shallow penetrometers in the range of 5-15 kPa, which spans the operating range for typical subsea pipelines.

Figure 7 shows the measured undrained penetration resistance for five hemiball and five toroid tests (for clarity only five tests are presented here for each device, although the unreported data sets yielded very similar results), with both devices approaching a similar failure load at the target embedment of w/D = 0.3. All shallow penetrometer tests yield comparable strength profiles, thus demonstrating high repeatability and resolution. The penetration rate required to ensure undrained conditions is significantly faster for the toroid due to its smaller diameter, thus leading to slightly more measurement noise, as can be seen in Figure 7 and Figure 8.

The procedure of Stanier & White (2014) was used to convert the measured vertical load, V, into the corresponding strength profiles. The inferred soil strength profiles, for both the toroid and hemiball penetrometer, are in excellent agreement with each other (Figure 8). Independent T-bar test measurements, with and without shallow corrections after White et al. (2010a), are plotted alongside the penetrometer tests to provide context. The shallow penetrometer measurements are bracketed by the strength profiles determined via the conventional uncorrected, assuming a bearing factor N_t = 10.5 (Stewart & Randolph, 1991), and the shallow corrected T-bar interpretation method.

Cyclic penetration

The purpose of the cyclic remoulding tests (CRT) is to emulate seabed disturbance such as the pipe laying process. Ten penetration-extraction cycles of 0.15D amplitude were conducted after the initial penetration to 0.3D, so with embedment depths ranging between ~0.15D and ~0.3D. Figure 9 shows that the penetration and extraction responses differ significantly for the two shallow penetrometer geometries tested. A major degradation of undrained strength and correspondingly large 'apparent' sensitivities, $S_t = s_u / s_{u,rem} >> 10$, were observed for both

penetrometers (Figure 10). This is much higher than found in comparative (deeply embedded) T-bar and ball cyclic penetrometer tests, for which S_t ~2.5.

It is clear from Figure 9 that the interpretation of strength degradation depends strongly on the adopted interpretation depth. All data points presented in Figure 10 were taken at the mid-depth of each cycle, as indicated in Figure 9 by the black markers. The bearing capacity factor, $N_{c,nom}$, required to estimate the undrained shear strength was assumed equal to that found for the initial monotonic penetration, at the same embedment depth and for all cycles. Results of a cyclic T-bar (diameter: 5 mm, length: 20 mm, N_t = 10.5) and a ball penetrometer test (diameter: 10 mm, N_b = 10.5 after Chung & Randolph, 2004) are plotted alongside the shallow penetrometer measurements for comparison purposes (Figure 10).

Close scrutiny of the excess pore pressure measurements revealed that water entrainment was most likely responsible for the massive strength degradation, as well as the formation of an indentation in the seabed. Near-zero pore pressure readings – indicative of break-away on extraction and subsequently water entrainment on re-penetration – are seen in Figure 11 for the invert transducer of the hemiball after only a few cycles of penetration.

It remains an open question as to which of the cyclic remoulding tests is most applicable for predicting the pipe-laying process: deep penetrometer tests such as the T-bar and ball penetrometer or the shallow penetrometer tests. Previous case studies of an offshore pipeline indicated that the 'as-laid' embedment was best predicted using the remoulded strength measured using a miniature T-bar, and this has been confirmed by a wider dataset (Westgate et al., 2012, White et al., 2017). The small amplitude movements of a shallow penetrometer test are more representative of the pipe-laying process, where water entrainment is highly probable (Sahdi et al., 2014), but the formation of a seabed indentation beneath the penetrometer hampers interpretation of data such as Figure 9. Given the experience using conventional T-bar penetrometer tests for as-laid embedment predictions, the role of cyclic shallow penetrometers tests is to provide additional information such as the dissipation characteristics following

remoulding and water entrainment, as well as the sliding friction determined during the rotation phase.

Pore pressure dissipation

The penetration stage is followed by a load-controlled (LC) consolidation phase. The aim in this study was to allow almost complete dissipation of the penetration induced excess pore pressures, with the vertical load applied to the penetrometer kept constant throughout at the load recorded at the final penetration depth, $V_{max} = f(w/D = 0.3)$, thereby simulating the self-weight of a pipe-like structure on the ocean floor. The duration of the consolidation phases were two and four hours for the toroid and hemiball penetrometer, respectively. A total of 8 toroid and 8 hemiball tests were carried out, although only the results of the latter 6 hemiball tests are presented here. This is because for the first two hemiball tests, silicone oil was used to backfill the pressure transducers, which resulted in clogging of the porous plastic filters used to shield the sensing elements, eventually leading to a drift in the pore pressure measurements. Investigation into different back-filling liquids revealed that de-aired water was least affected by clogging in fine-grained sediments (Schneider et al., 2019a).

The excess pore pressure measurements were interpreted using the methodology described earlier and the model coefficients given in Table 2 & Table 4, with both penetrometers yielding very similar coefficients of consolidation, c_{v0}. This is in spite of the fact that the dimensional dissipation response for the toroid is significantly faster than for the hemiball, due to the four-fold difference in device cross-sectional dimensions. This is evidence of the robustness of the interpretation model proposed. Figure 12 shows a summary of the values inferred from the different dissipation solutions stated in Table 2 and Table 4 (including c_{v0}-values obtained from dissipation measurements following both a monotonic and a cyclic penetration stage).

Excellent test repeatability is evident for the dissipation response. Most inferred coefficients of consolidation lie within a relatively close range of c_{v0} = 4-8 m^2/yr, irrespective of the device used, with only the values corresponding to the invert response of the hemiball deviating from

this range. The SSFE wished-in-place dissipation solutions published by Yan et al. (2017) yield almost identical values to the LDFE solutions presented by Chatterjee et al. (2012) and the hemiball solutions provided in this paper, in spite of the LDFE simulations better capturing peripheral soil heave. This confirms that soil heave around the periphery of the penetrometers has minimal influence on the dissipation characteristics. The fact that very similar c_{v0}-values were found for both test variations (monotonic or cyclic penetration prior to dissipation), suggests that the remoulding cycles seemed to affect the soil only very locally (close to the probe interface). The coefficient of consolidation inferred therefore seems to be governed mainly by the intact soil state rather than by the remoulded condition.

A good match between the shapes of the numerically (SSFE and LDFE) and experimentally derived dissipation responses was found for both penetrometers and all transducer locations (e.g. Illustration of back-analysis procedure after Stanier & White (2014) for a toroid test: (a) bearing capacity factor model fit; and (b) the derived undrained strength profile.

Figure 4c), except for the invert position of the hemiball, where a noticeable difference in shape was encountered. Moreover, there is no measurement redundancy for this position as there can only be a single pressure sensor there. Consequently, we recommend using the LDFE dissipation solutions corresponding to the invert and intermediate locations for the toroid and hemiball, respectively, and taking advantage of averaging through the use of multiple transducers. The readings recorded by the midface hemiball transducers are often negatively affected by the proximity to the mudline. However, if the penetrometer is sufficiently embedded, the midface measurements can also provide independent estimates of the coefficient of consolidation.

Figure 13 compares the inferred coefficients of consolidation with miniature piezocone (c_h) and Rowe cell data (c_v) measured independently in the same kaolin clay over the past decade or more at UWA (Richardson et al., 2007, Chow et al., 2014; Cocjin et al., 2014). Data at shallow embedment is conspicuously absent, but the shallow penetrometer data presented here is

consistent with the measurements generated using the 'parkable piezoprobe', another device intended to measure surficial soil properties (Chatterjee et al., 2014; Schneider et al., 2018) and the back-extrapolated trends from the piezocone and Rowe cell data.

CONCLUSIONS

This paper has shown that the strength and consolidation properties of soft surficial soil can be estimated reliably with shallow penetrometers, such as the box-core sized toroid and hemiball. The fundamentals of the penetration and dissipation stage, alongside the geotechnical relationships needed to back-analyse such tests, were highlighted. Furthermore, new large deformation finite element (LDFE) dissipation solutions, exploring the impact of local peripheral heave on the dissipation response for the hemiball and a comprehensive laboratory testing programme in kaolin clay were presented. The key findings can be summarised as:

- Results of the laboratory testing session demonstrate that both penetrometers are capable of providing accurate estimates of undrained strength and consolidation characteristics of fine-grained surficial sediments. Excellent test repeatability was demonstrated and the interpretation models were shown to be robust, with all results in excellent agreement with each other and consistent with the existing literature.
- Simple interpretations of the undrained soil strength profiles can be obtained for design purposes using the model of Stanier & White (2014). The methodology yields very comparable results to miniature T-bar measurements.
- Back-analysis of the experiments demonstrates that the LDFE hemiball dissipation solutions presented here yield consistent estimates for the coefficient of consolidation. Additional outcomes include (a) the preferred use of the pore pressure measurements recorded at the intermediate hemiball transducer location and (b) the observation that soil heave around the periphery of the penetrometers has minimal influence on the dissipation response.

- Deeper insight into the effect of the pipe laying process can be gained by executing undrained penetration / extraction cycles. The extreme strength degradation observed in these tests warrants further exploration of the potential impact of water entrainment during pipe-laying in estimating pipeline embedment. An experimental study investigating the influence of the cycling rate and amplitudes on the strength, deformation and dissipation characteristics of fine-grained soils would be a logical next step. Consequently, it is suggested that a conventional miniature full-flow penetrometer continue to be used to assess soil sensitivity, rather than a cyclic shallow penetrometer test.

ACKNOWLEDGEMENTS

The research presented here forms part of the activities of the Centre for Offshore Foundation Systems (COFS), currently supported as a node of the Australian Research Council Centre of Excellence for Geotechnical Science and Engineering (CE110001009). The first author is grateful for the support provided by an International Postgraduate Research Scholarship (IPRS) from the Australian Government. The second author was supported by an ARC DECRA Fellowship (DE170100119). This work has been further supported by Shell, via the Shell EMI Chair in Offshore Engineering held by the third author, and by Fugro via the Fugro Chair in Geotechnics held by the fourth author. The authors are also grateful for the support from the RIGSS JIP partners: Fugro, Shell, Total and Woodside Energy.

NOTATION

A_{nom}	nominal area
c_h	operative coefficient of consolidation
c_v	coefficient of consolidation
c_{v0}	initial coefficient of consolidation at penetrometer invert
D	device diameter
D_{Tbar}	diameter of T-bar penetrometer
e_0	initial void ratio
e_{cs}	void ratio on critical state line at p'=1kPa
f_b	soil buoyancy factor
K_0	coefficient of earth pressure at rest
k	soil permeability
k_{su}	gradient of undrained strength profile
L	lever arm (toroid penetrometer)
M	slope of critical state line in q-p' space
m	fitting parameter (dissipation solution)
m_{ave}	fitting parameter (periphery consolidation solution)
m_v	coefficient of volume compressibility
N	cycle number (cyclic remoulding test)
N_b	bearing capacity factor for ball penetrometer
$N_{c,nom}$	bearing capacity factor
N_t	bearing capacity factor for T-bar
OCR	over-consolidation ratio
p'	mean effective stress
p_0'	initial mean effective stress
q_0	surcharge at mudline
S_t	soil sensitivity
s_u	undrained shear strength
$s_{u,avg}$	average undrained shear strength
s_{u0}	undrained shear strength at penetrometer invert
$s_{u,c}$	consolidated undrained shear strength
$s_{u,m}$	undrained shear strength at mudline
$s_{u,rem}$	remoulded undrained shear strength
T	mobilised torque
T_{dis}	dimensionless time (dissipation stage)
$T_{dis,50}$	dimensionless time at ~50% consolidation
$T_{dis,50,ave}$	dimensionless time at ~50% consolidation (periphery dissipation)
t	time
t_{dis}	dissipation time
u	pore water pressure
V	vertical penetration resistance
V_b	resistance due to soil buoyancy
V_{geot}	geotechnical resistance
V_{max}	bearing capacity load (end of penetration stage)
V_{pen}	dimensionless velocity (penetration stage)
V_s	embedded penetrometer volume (relative to original mudline)

v_{pen}	vertical penetration speed
w	embedment depth

γ'	effective unit weight
γ_w	unit weight of water
Δu	excess pore water pressure
Δu_{ave}	average excess pore pressure of different transducer readings
Δu_{ini}	initial excess pore water pressure at consolidation start
δ	drained interface friction angle
θ	local inclination regarding vertical
κ	slope of elastic compression line
λ	slope of virgin compression line
ν	Poisson ratio
ϕ'	angle of internal friction
ϕ'_{cv}	constant volume friction angle
ψ	drainage index

REFERENCES

Baligh, M. M., Azzouz, A. M. & Chin, C.-T. (1987). Disturbances due to 'ideal' tube sampling. *J. Geotech. Engrg.* **113**, No. 7, 739-757.

Chatterjee, S., Randolph, M. F. & White, D. J. (2014). A parkable piezoprobe for measuring c_v at shallow depths for offshore design, *Géotechnique* **64**, No. 1, 83-88.

Chatterjee, S., White, D. J. & Randolph, M. F. (2013). Coupled consolidation analysis of pipe–soil interactions. *Canadian Geotechnical Journal* **50**, No. 6, 609-619.

Chatterjee, S., Yan, Y., Randolph, M. F. & White, D. J. (2012). Elastoplastic consolidation beneath shallowly embedded offshore pipelines, *Géotechnique Letters*, No. 2, 73-79.

Chow, S. H., O'Loughlin, C. D. & Randolph, M. F. (2014). Soil strength estimation and pore pressure dissipation for free-fall piezocone in soft clay. *Géotechnique* **64**, No. 10, 817-827.

Chung, S. F. & Randolph, M. F. (2004). Penetration resistance in soft clay for different shaped penetrometers. *Proceedings 2nd International Conference on Site Characterisation*, Porto **2**, No. 1, 671-678.

Clayton, C. R. I., Siddique, A. & Hopper, R. J. (1998). Effects of sampler design on tube sampling disturbance – numerical and analytical investigations. *Géotechnique* **48**, No. 6, 847-867.

Cocjin, M. J., Gourvenec, S. M., White, D. J. & Randolph, M. F. (2014). Tolerably mobile subsea foundations–observations of performance. *Géotechnique* **64**, No. 11, 895-909.

Cryer, C. W. (1963). A comparison of the three dimensional consolidation theories of Biot and Terzaghi. *Q. J. Mech. Appl. Math.* **16**, No. 4, 401-412.

Dassault Systèmes. (2011). Abaqus analysis user's manual. Simulia Corporation. Providence, RI, USA.

Det Norsek Veritas. (2007). DNV-RP-F110 - Global buckling of submarine pipelines.

Finnie, I. M. S. (1993). Performance of Shallow Foundations in Calcareous Soil. PhD thesis, The University of Western Australia, Australia.

Finnie, I. M. S. & Randolph, M. F. (1994). Punch-through and liquefaction induced failure of shallow foundations on calcareous sediments. *Proc. Int. Conf. Behav. Offshore Struct. (BOSS)*, Boston, Machachusetts, 2017-230.

Hover, E. D., Ni, Q. & Guymer, I. (2013). Investigation of centreline strain path during tube penetration using transparent soil and particle image velocimetry. *Géotechnique Letters* **3**, No. 2, 37-41.

Hu, Y. & Randolph, M. F. (1998). A practical numerical approach for large deformation problems in soil. *International Journal of Numerical and Analytical Methods in Geomechanics* **22**, No. 5, 327-350.

Kuo, M. Y.-H., Vincent, C. M., Bolton, M. D., Hill, A. & Rattley, M. (2015). A new torsional shear device for pipeline interface shear testing. *Frontiers in Offshore Geotechnics III – Meyer (Ed.)*, 405-410.

Lehane, B. M. & Liu, Q. B. (2013). Measurement of shearing characteristics of granular materials at low stress levels in a shear box. *Geotechnical and Geological Engineering*, No. 31, 329-336.

Mandel, J. (1950). Étude mathématique de la consolidation des sols. *Actes du Colloque International de Mécanique, Poitier, France* **4**, 9-19.

Meyer, V., Dyvik, R. & White, D. J. (2015). Direct shear interface tests for pipe-soil interaction assessment. *Frontiers in Offshore Geotechnics III – Meyer (Ed.)*, 423-428.

Morton, J. P., O'Loughlin, C. D. & White, D. J. (2014). Strength assessment during shallow penetration of a sphere in clay. *Géotechnique Letters* **4**, 262-266.

Pedersen, R., Olson, R. & Rauch, A. (2003). Shear and interface strength of clay at very low effective stress. *Geotechnical Testing Journal* **26**, No. 1, 71-78.

Pineda, J. A., Liu, X. F. & Sloan, S. W. (2016). Effects of tube sampling in soft clay: a microstructural insight. *Géotechnique* **66**, No. 12, 969-983.

Randolph, M. F., Stanier, S. A., O'Loughlin, C. D., Chow, S. H., Bienen, B., Doherty, J. P., Mohr, H., Ragni, R., Schneider, M. A., White, D. J. & Schneider, J. A. (2018). Penetrometer equipment and testing techniques for offshore design of foundations, anchors and pipelines. *CPT'18 – International Symposium on Cone Penetration Testing*, Delft.

Richardson, M. (2007). Rowe cell test on kaolin clay, COFS internal report. Centre for Offshore Foundation Systems, UWA, Crawley, Western Australia.

Roscoe, K. H. & Burland, J. B. (1968). On the generalized stress-strain behaviour of wet clay. *In: Engineering Plasticity*, Cambridge: 535-609.

Sahdi, S., Gaudin, C. & White, D. J. (2014). Strength properties of ultra-soft kaolin. *Canadian Geotechnical Journal* **51**, 420-431.

Schneider, M. A., Stanier, S. A., Chatterjee, S., White, D. J. & Randolph, M. F. (2018). The parkable piezoprobe for determining c_v and strength – modelling and interpretation methods. *Accepted for publication by Géotechnique*.

Schneider, M. A., Stanier, S. A., White, D. J. & Randolph, M. F. (2019a). Apparatus for measuring pipe-soil interaction behaviour using shallow 'pipe-like' penetrometers. *Submitted to Geotechnical Testing Journal*.

Schneider, M. A., Stanier, S. A., White, D. J. & Randolph, M. F. (2019b). Shallow penetrometer tests – Theoretical and experimental modelling of the rotation stage. *Accepted for publication by Canadian Geotechnical Journal*.

Stanier, S. A. & White, D. J. (2014). Shallow penetrometer penetration resistance. *Journal of Geotechnical and Geoenvironmental Engineering* **141**, No. 3, 04014117.

Stewart, D. P. & Randolph M. F. (1991). A new site investigation tool for the centrifuge. *In Proceedings of the International Conference on Centrifuge Modelling*, Boulder, Colorado, 13-14 June 1991. Balkema, Rotterdam, the Netherlands. pp. 531-538.

Stewart, D. P. (1992). Lateral loading of piled bridge abutments due to embankment construction. PhD thesis, University of Western Australia.

Sully, J. P., Robertson, P. K., Campanella, R. G. & Woeller, D. J. (1999). An approach to evaluation of field CPTU dissipation data in overconsolidated fine-grained soils. *Canadian Geotechnical Journal* **36**, No. 2, 369-381.

Taiebat, H. A. & Carter, J. P. (2008). Flow rule effects in the Tresca model. *Computers and Geotechnics* **35**, 500-503.

Tapper, L., Martin, C. M. & Byrne, B. W. (2014). Undrained bearing capacity of circular footings on Tresca soil using adaptive finite element analysis. *Numerical Methods in Geotechnical Engineering*, Vol 1.

Vermeer, P. A. & Verruijt, A. (1981). An accuracy condition for consolidation by finite elements. *International Journal for Numerical and Analytical Methods in Geomechanics* **5**, No. 1, 1-14.

Wang, D., White, D. J. & Randolph, M. F. (2010). Large-deformation finite element analysis of pipe penetration and large-amplitude lateral displacement. *Canadian Geotechnical Journal* **47**, No. 8, 842-856.

Westgate, Z. J., White, D. J. & Randolph, M. F. (2012). Field observations of as-laid pipeline embedment in carbonate sediments. *Géotechnique* **62**, No. 9, 787-798.

Westgate, Z. J., White, D. J. & Savazzi, M. (2018). Experience with interface shear box testing for axial pipe-soil interaction assessment on soft clay. *Proceedings Offshore Technology Conference*, Paper OTC-28671-MS.

White, D. J., Gaudin, C., Boylan, N. & Zhou, H. (2010a). Interpretation of T-bar penetrometer tests at shallow embedment and in very soft soils. *Canadian Geotechnical Journal* **47**, No. 2, 218-229.

White, D. J., Hill, A. J., Westgate, Z. J. & Ballard, J-C. (2010b). Observations of pipe-soil response from the first deep water deployment of the SMARTPIPE. *Frontiers in Offshore Geotechnics II – Gourvenec & White (eds)*, 851-856.

White, D. J., Clukey, E. C., Randolph, M. F., Boylan, N. P., Bransby, M. F., Zakeri, A., Hill, A. J. & Jaeck, C. (2017). The state of knowledge of pipe-soil interaction for on-bottom pipeline design, *Proceedings Offshore Technology Conference*, OTC 27623.

Wood, D. M. (1990). *Soil behaviour and critical state soil mechanics.* Cambridge university press.

Yan, Y., White, D. J. & Randolph, M. F. (2011a). Penetration resistance and stiffness factors for hemispherical and toroidal penetrometers in uniform clay. *International Journal of Geomechanics* **11**, No. 4, 263-275.

Yan, Y., White, D. J. & Randolph, M. F. (2011b). Investigations into novel shallow penetrometers for fine-grained soils. *Frontiers in Offshore Geotechnics II – Gourvenec & White (eds)*, 321-326.

Yan, Y., White, D. J. & Randolph, M. F. (2017). Elastoplastic consolidation solutions for scaling from shallow penetrometers to pipelines. *Canadian Geotechnical Journal* **54**, No. 6, 881-895.

Yan, Y. (2014). Novel methods for characterising pipe-soil interaction forces in-situ in deep water. PhD thesis, The University of Western Australia, Australia.

Zienkiewicz, O. C. & Zhu, J. Z. (1992). The superconvergent patch recovery and a posteriori error estimates. Part 1: The recovery technique. *International Journal for Numerical Methods in Engineering* **33**, No. 7, 1331-1364.

LIST OF FIGURES

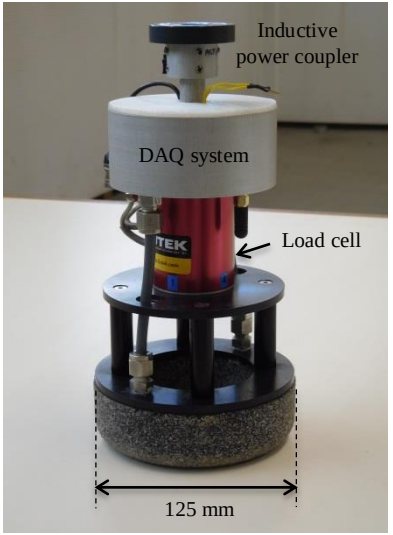

(a)

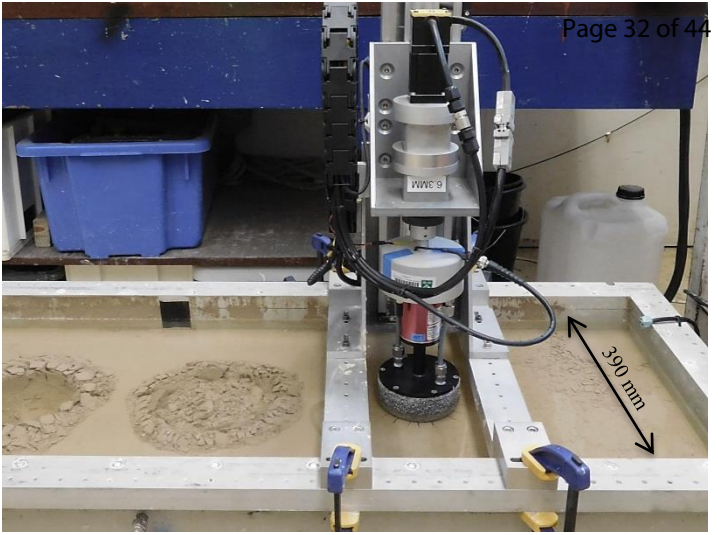

(b)

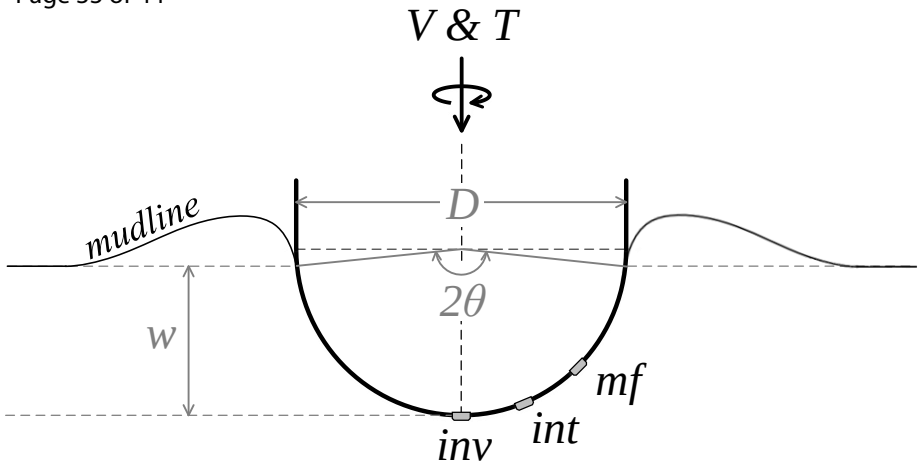

(a)

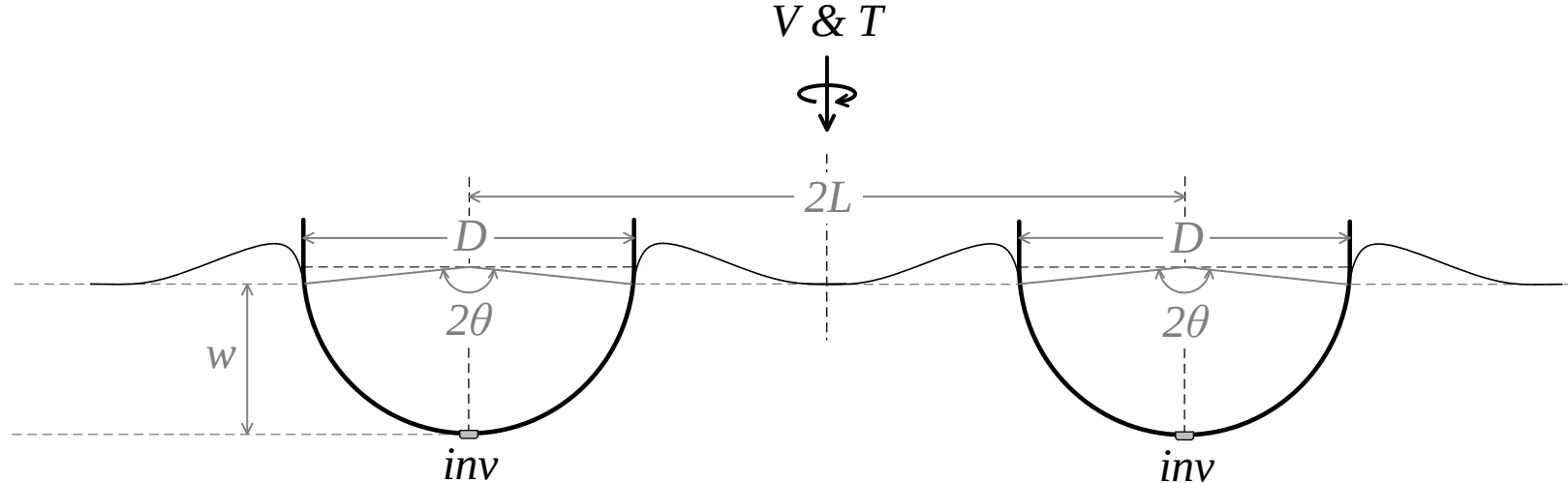

(b)

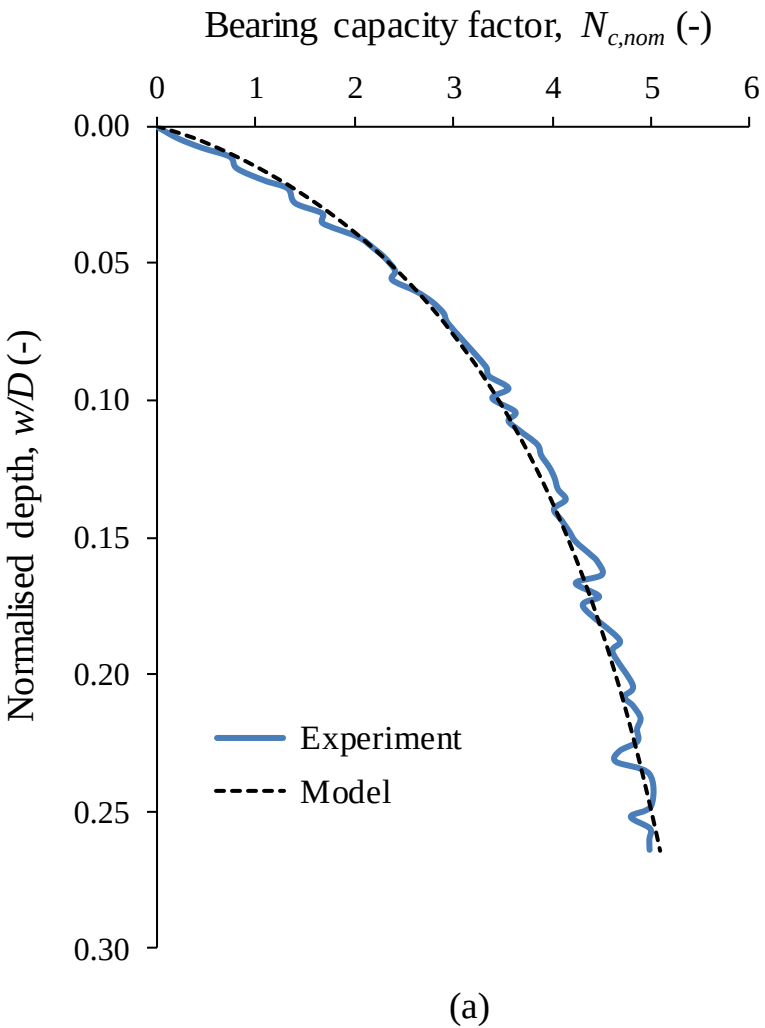
Bearing capacity factor, $N_{c,nom}$ (-)
0
1
2
3
4
5
6
0.00
0.05
0.10
0.15
0.20
0.25
0.30
Normalised depth, w/D (-)
Experiment
Model

(a)

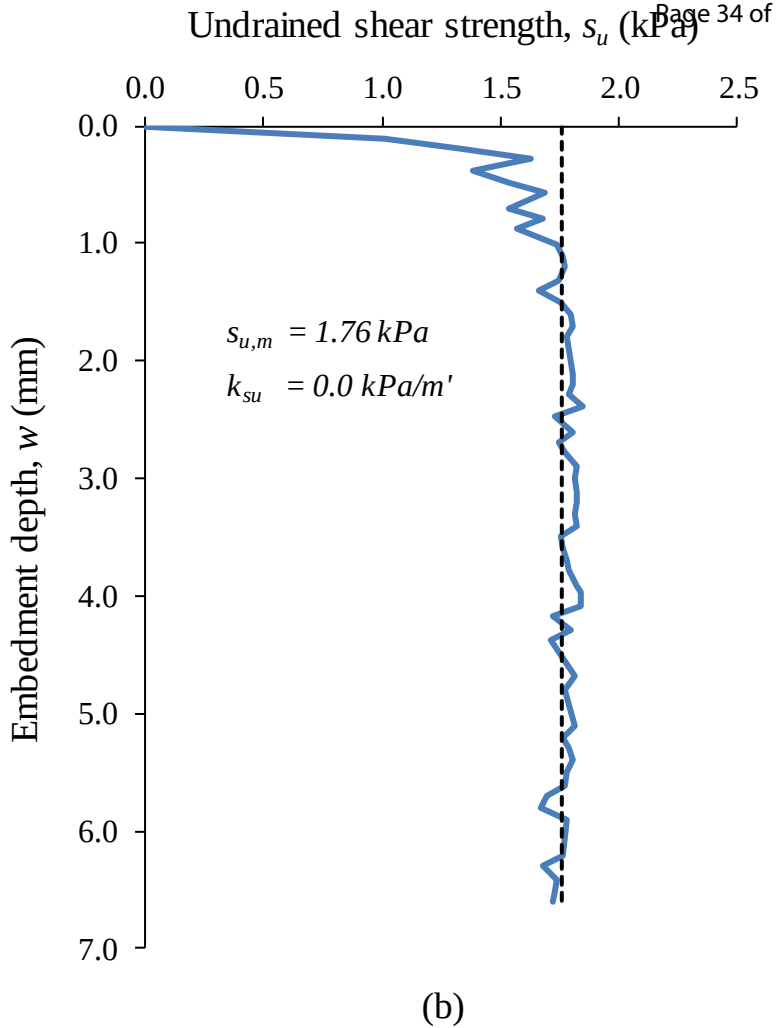
Undrained shear strength, s_u (kPa)
0.0
0.5
1.0
1.5
2.0
2.5
0.0
1.0
2.0
3.0
4.0
5.0
6.0
7.0
Embedment depth, w (mm)
$s_{u,m}$ = 1.76 kPa
k_{su} = 0.0 kPa/m'

(b)

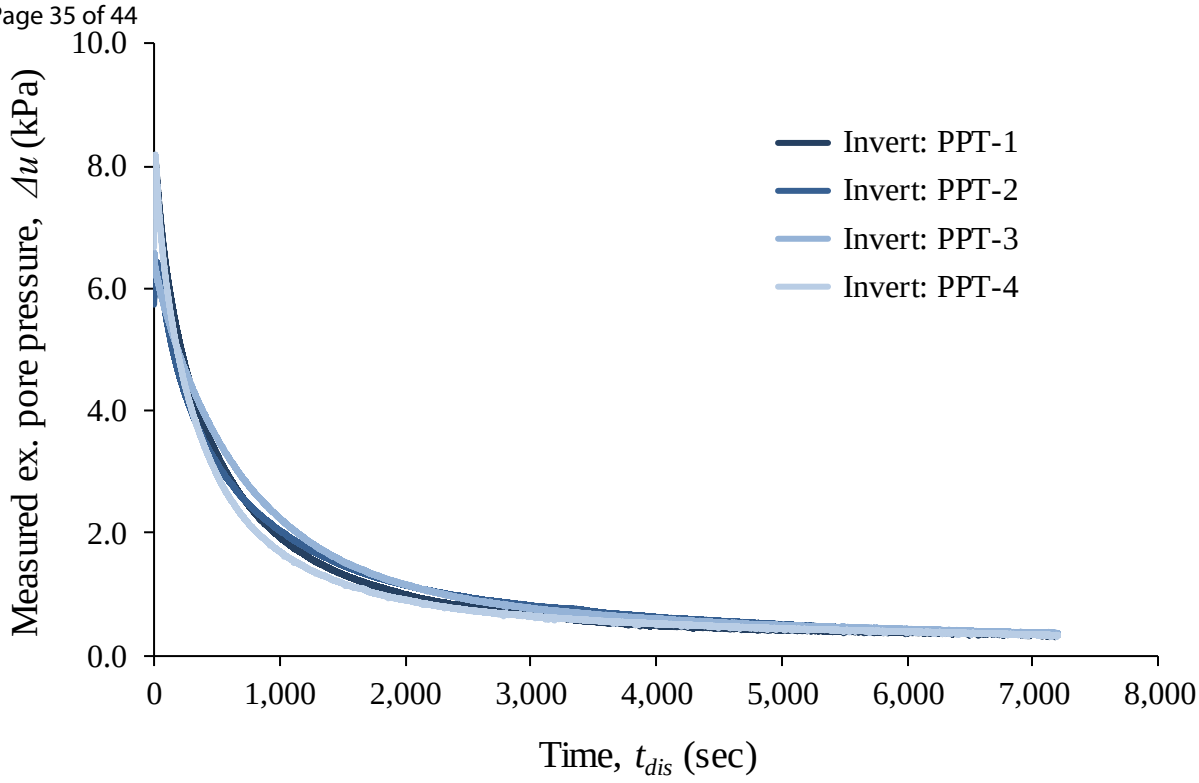
Measured ex. pore pressure, Δu (kPa)
10.0
8.0
6.0
4.0
2.0
0.0
0
1,000
2,000
3,000
4,000
5,000
6,000
7,000
8,000
Time, t_{dis} (sec)
Invert: PPT-1
Invert: PPT-2
Invert: PPT-3
Invert: PPT-4

(a)

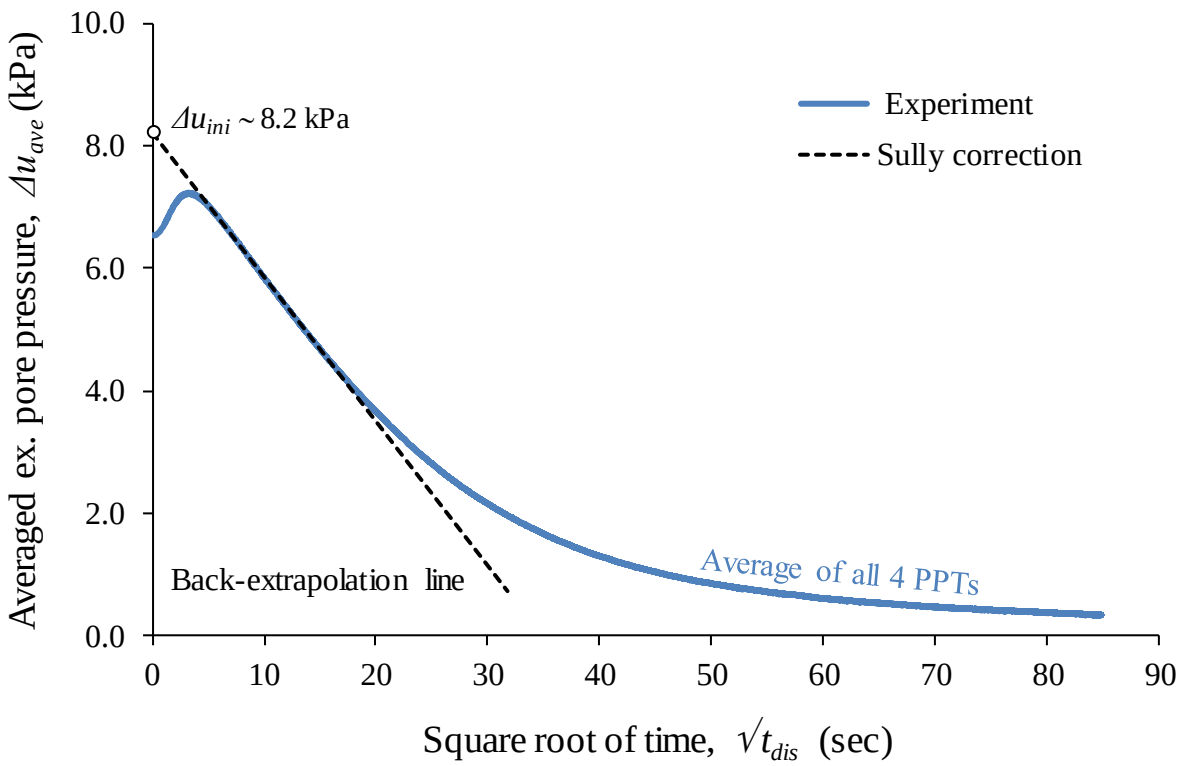
Averaged ex. pore pressure, Δu_{ave} (kPa)
10.0
8.0
6.0
4.0
2.0
0.0
0
10
20
30
40
50
60
70
80
90
Square root of time, $\sqrt{t_{dis}}$ (sec)
Δu_{ini} ~ 8.2 kPa
Experiment
Sully correction
Back-extrapolation line
Average of all 4 PPTs

(b)

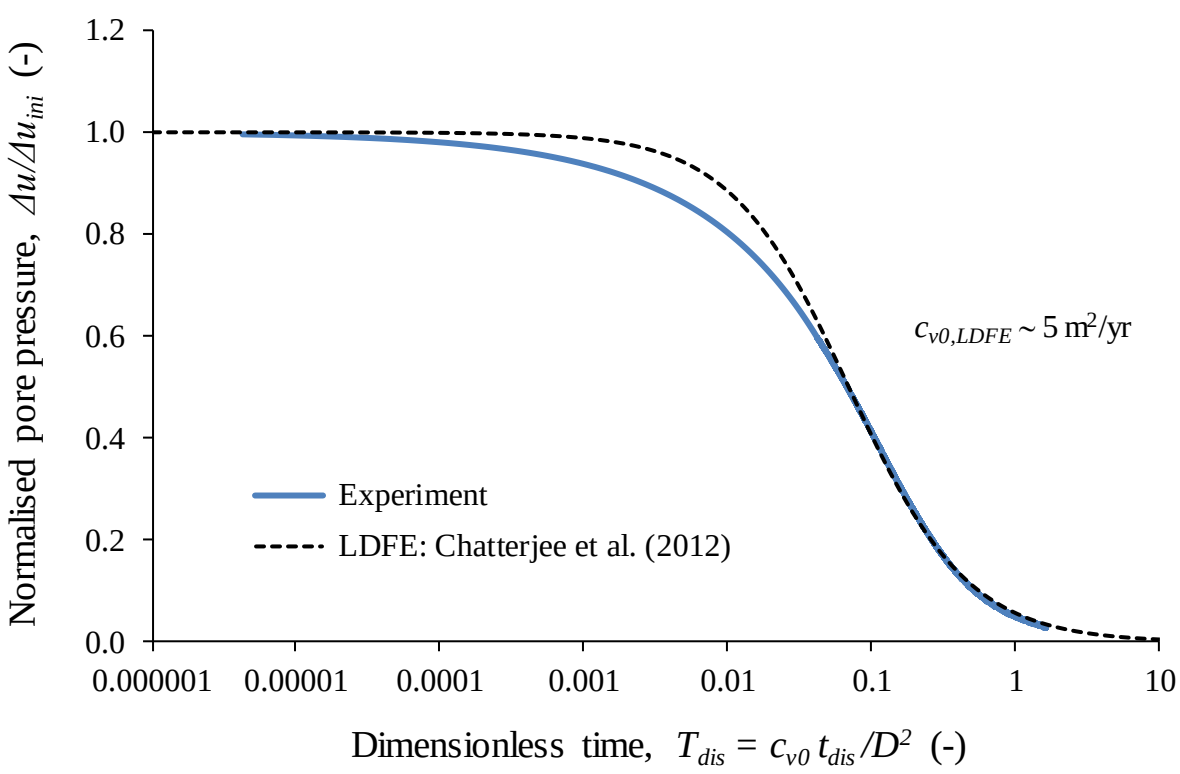
Normalised pore pressure, $\Delta u/\Delta u_{ini}$ (-)
1.2
1.0
0.8
0.6
0.4
0.2
0.0
0.000001
0.00001
0.0001
0.001
0.01
0.1
1
10
Dimensionless time, $T_{dis} = c_{v0}\, t_{dis}/D^2$ (-)
$c_{v0,LDFE}$ ~ 5 m^2/yr
Experiment
LDFE: Chatterjee et al. (2012)

(c)

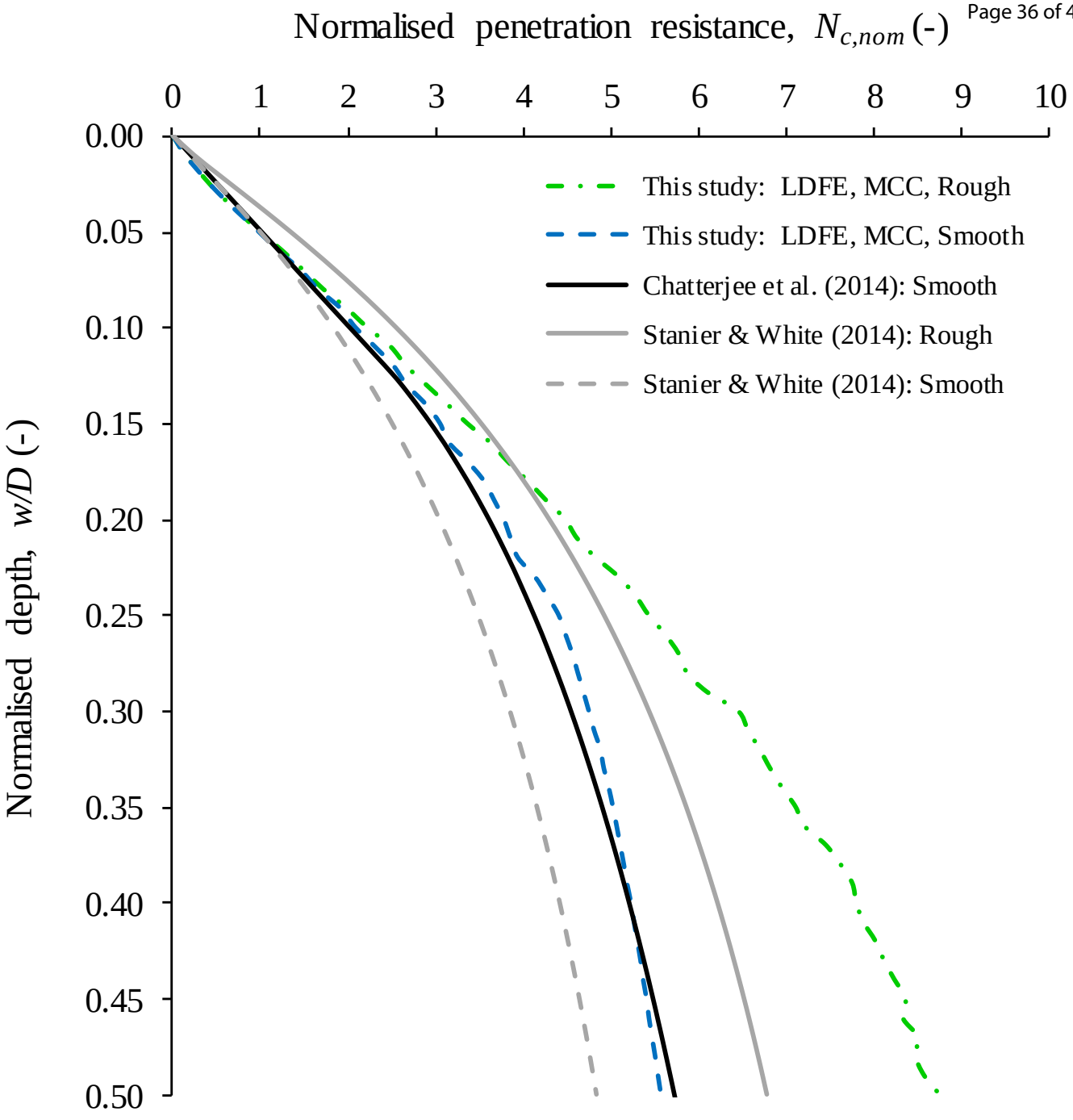
Normalised penetration resistance, $N_{c,nom}$ (-)
0
1
2
3
4
5
6
7
8
9
10
0.00
0.05
0.10
0.15
0.20
0.25
0.30
0.35
0.40
0.45
0.50
Normalised depth, w/D (-)
This study: LDFE, MCC, Rough
This study: LDFE, MCC, Smooth
Chatterjee et al. (2014): Smooth
Stanier & White (2014): Rough
Stanier & White (2014): Smooth

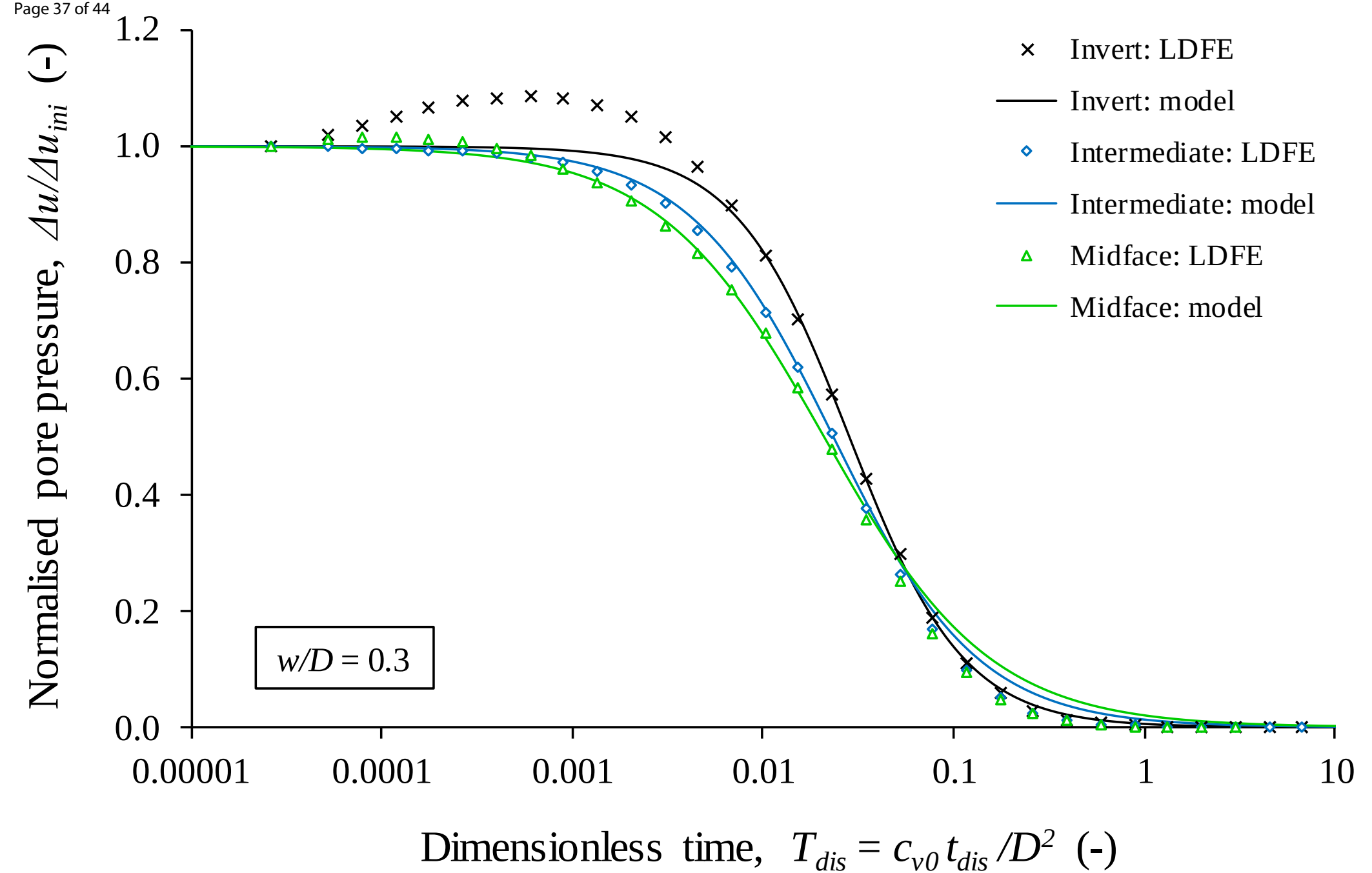
Normalised pore pressure, $\Delta u/\Delta u_{ini}$ (-)
1.2
1.0
0.8
0.6
0.4
0.2
0.0
0.00001
0.0001
0.001
0.01
0.1
1
10
Dimensionless time, $T_{dis} = c_{v0}\, t_{dis}\, /D^2$ (-)
Invert: LDFE
Invert: model
Intermediate: LDFE
Intermediate: model
Midface: LDFE
Midface: model
w/D = 0.3

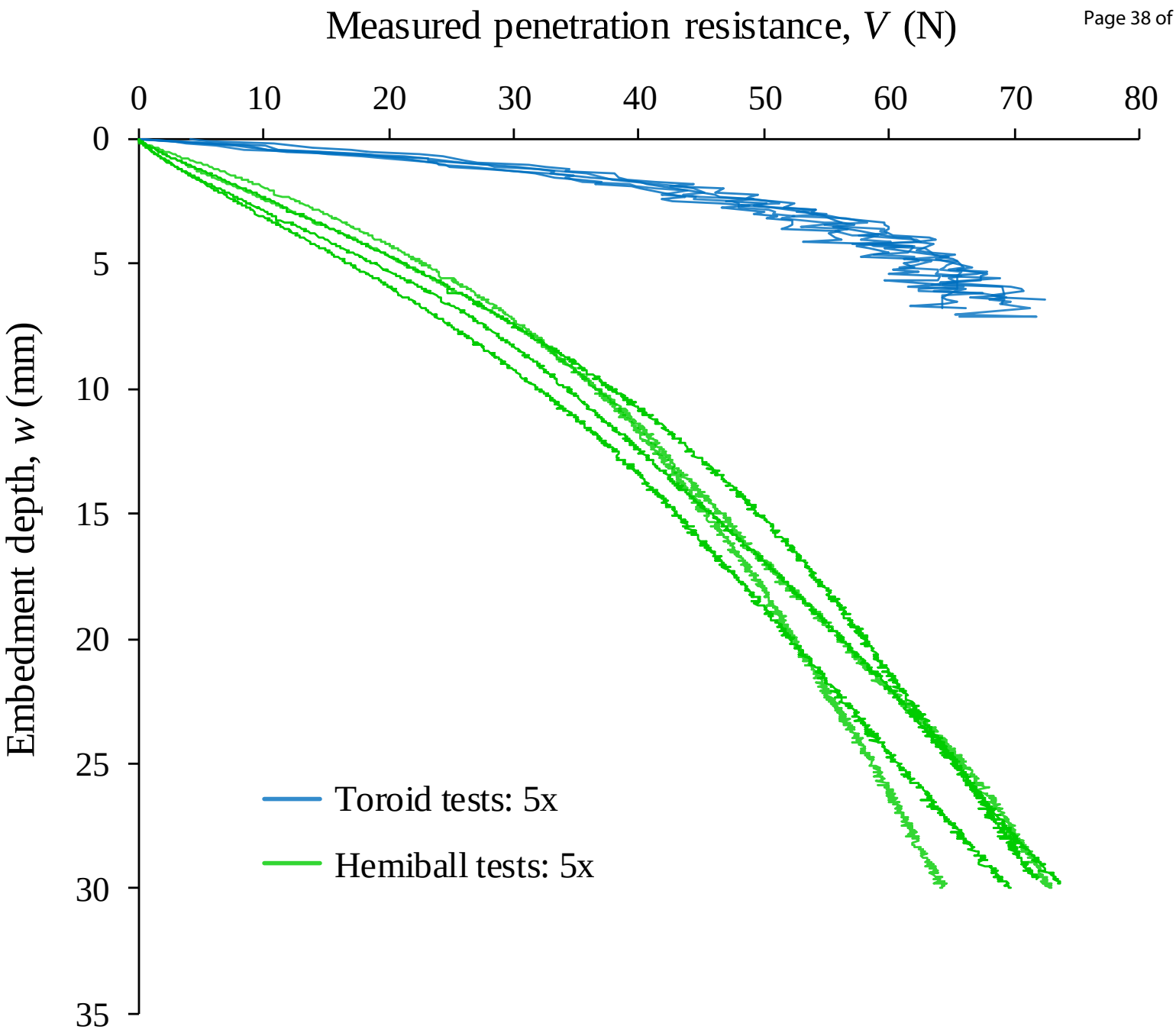
Measured penetration resistance, V (N)
0
10
20
30
40
50
60
70
80
Embedment depth, w (mm)
0
5
10
15
20
25
30
35
Toroid tests: 5x
Hemiball tests: 5x

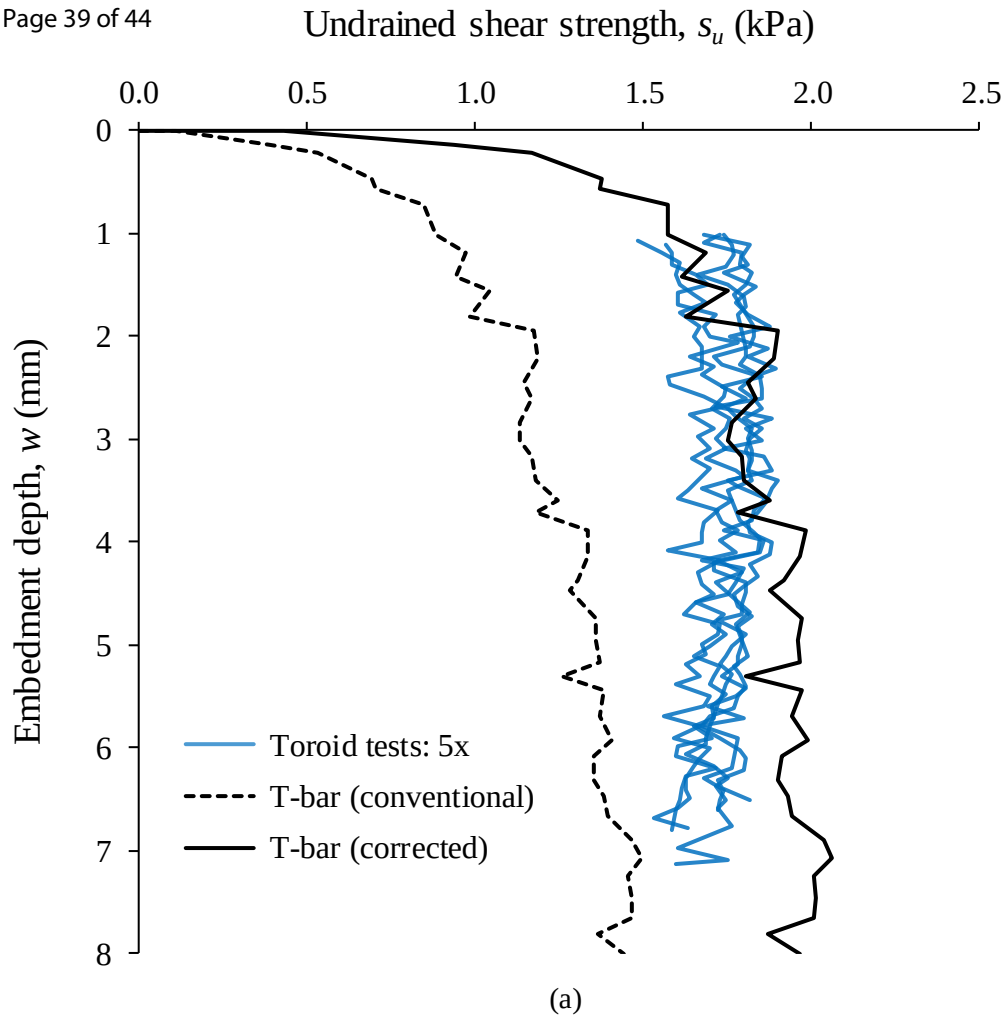
Undrained shear strength, s_u (kPa)
0.0
0.5
1.0
1.5
2.0
2.5
0
1
2
3
4
5
6
7
8
Embedment depth, w (mm)
Toroid tests: 5x
T-bar (conventional)
T-bar (corrected)

(a)

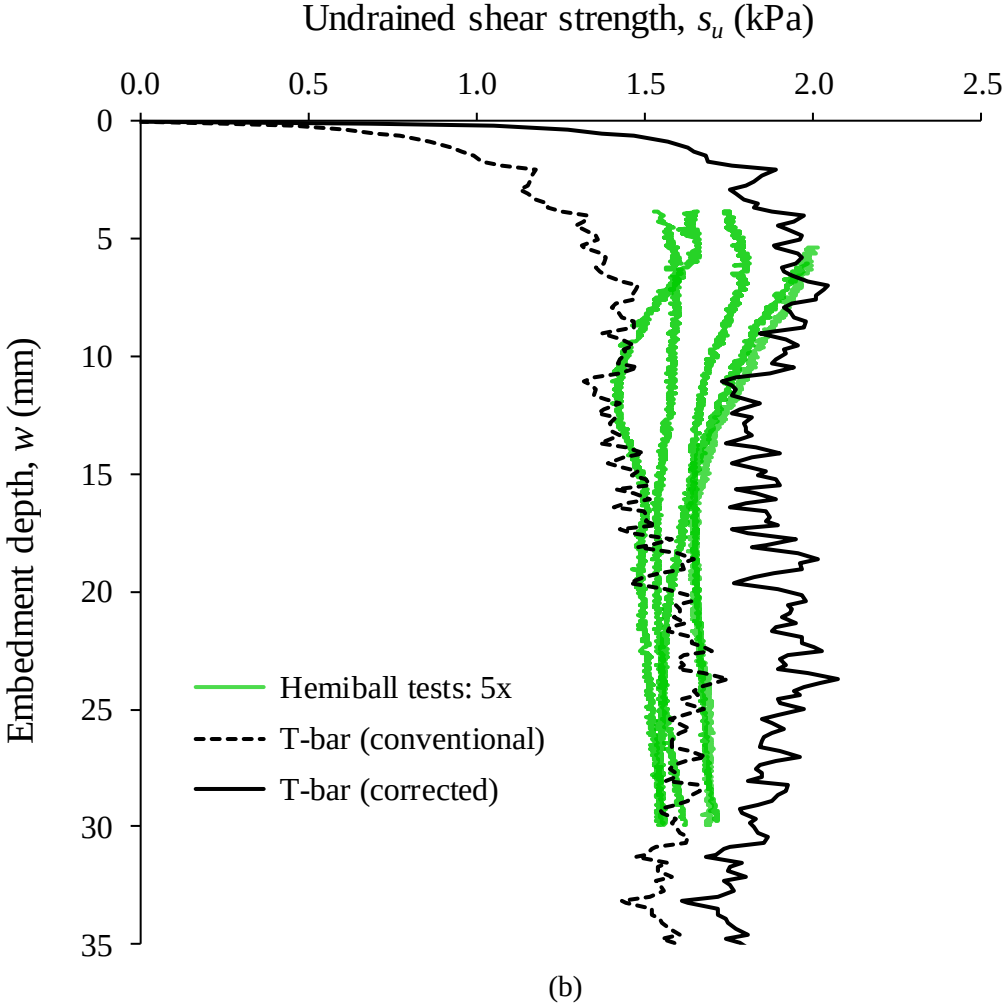
Undrained shear strength, s_u (kPa)
0.0
0.5
1.0
1.5
2.0
2.5
0
5
10
15
20
25
30
35
Embedment depth, w (mm)
Hemiball tests: 5x
T-bar (conventional)
T-bar (corrected)

(b)

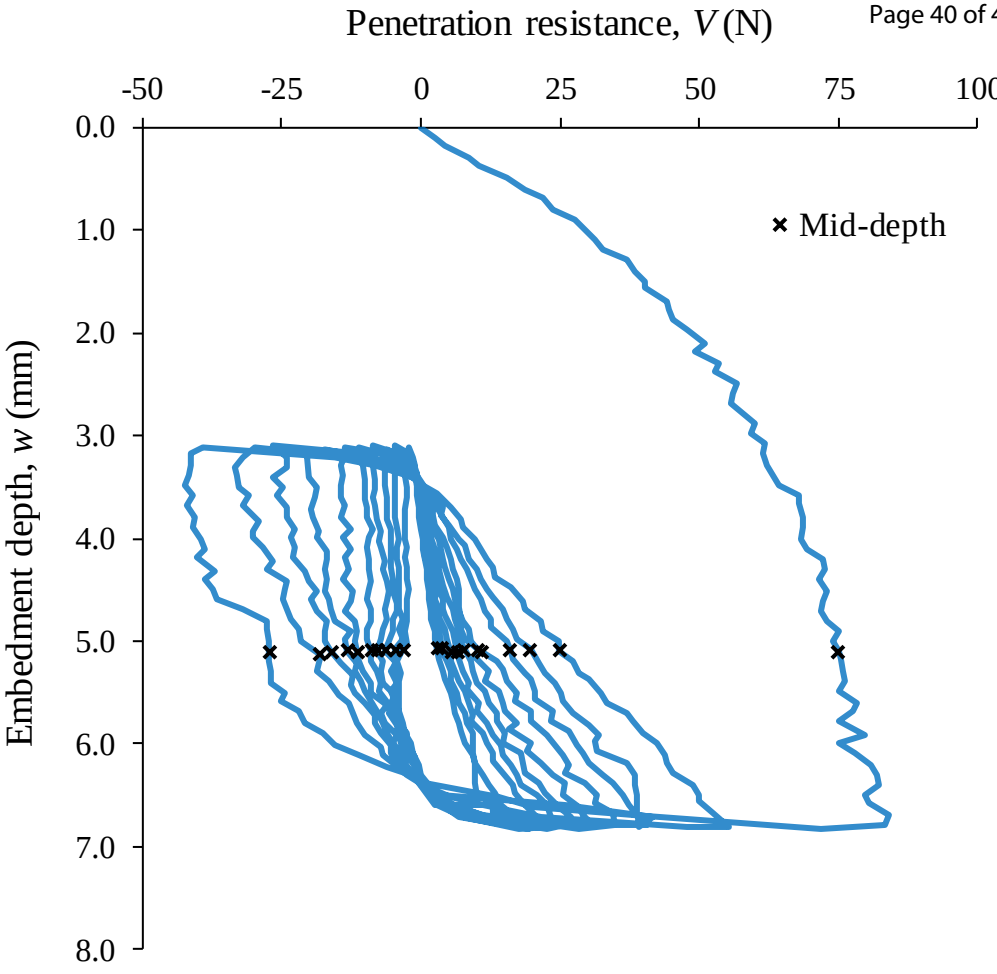
Penetration resistance, V (N)
-50
-25
0
25
50
75
100
0.0
1.0
2.0
3.0
4.0
5.0
6.0
7.0
8.0
Embedment depth, w (mm)
Mid-depth

(a)

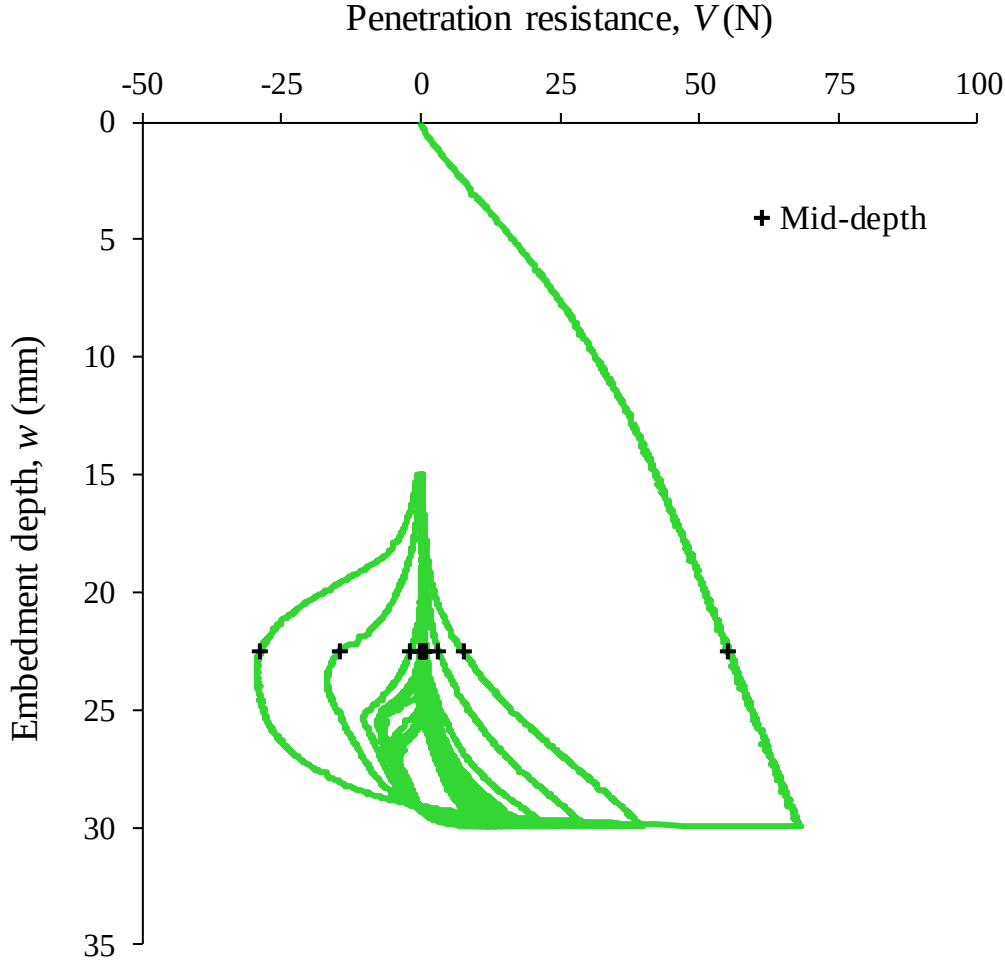
Penetration resistance, V (N)
-50
-25
0
25
50
75
100
0
5
10
15
20
25
30
35
Embedment depth, w (mm)
Mid-depth

(b)

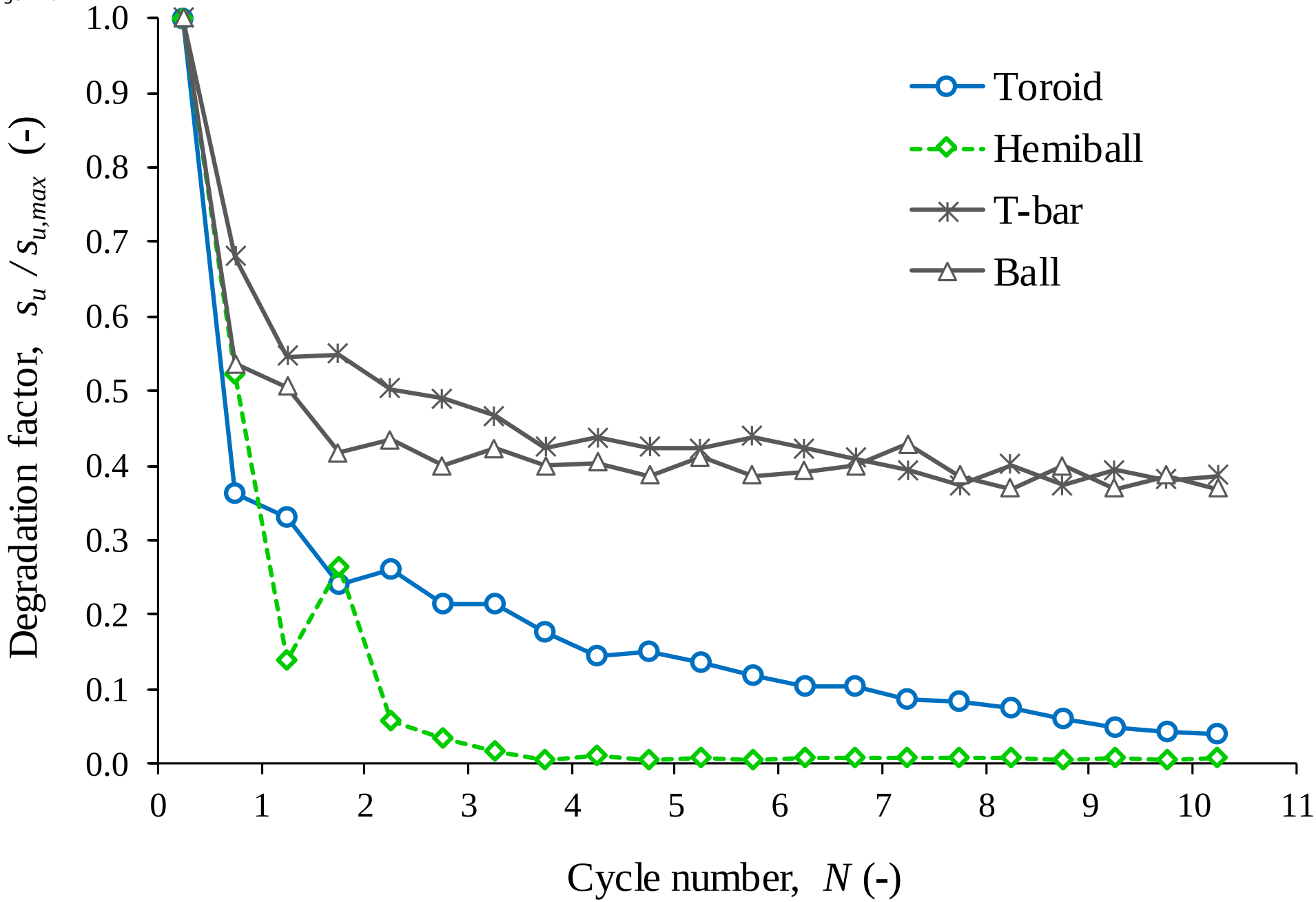
Degradation factor, $s_u / s_{u,max}$ (-)
1.0
0.9
0.8
0.7
0.6
0.5
0.4
0.3
0.2
0.1
0.0
0
1
2
3
4
5
6
7
8
9
10
11
Cycle number, N (-)
Toroid
Hemiball
T-bar
Ball

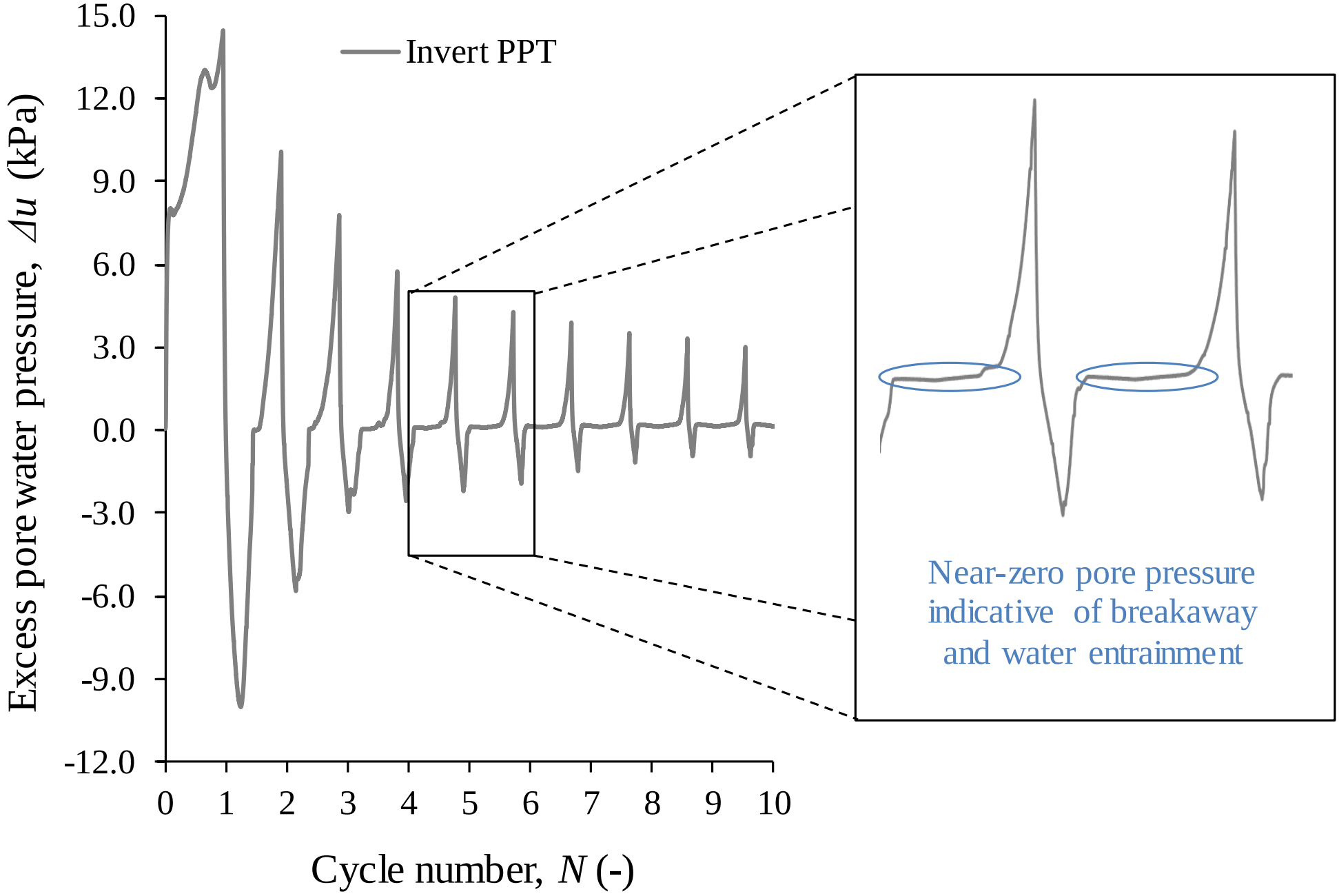
Invert PPT
Excess pore water pressure, Δu (kPa)
15.0
12.0
9.0
6.0
3.0
0.0
-3.0
-6.0
-9.0
-12.0
0
1
2
3
4
5
6
7
8
9
10
Cycle number, N (-)
Near-zero pore pressure indicative of breakaway and water entrainment

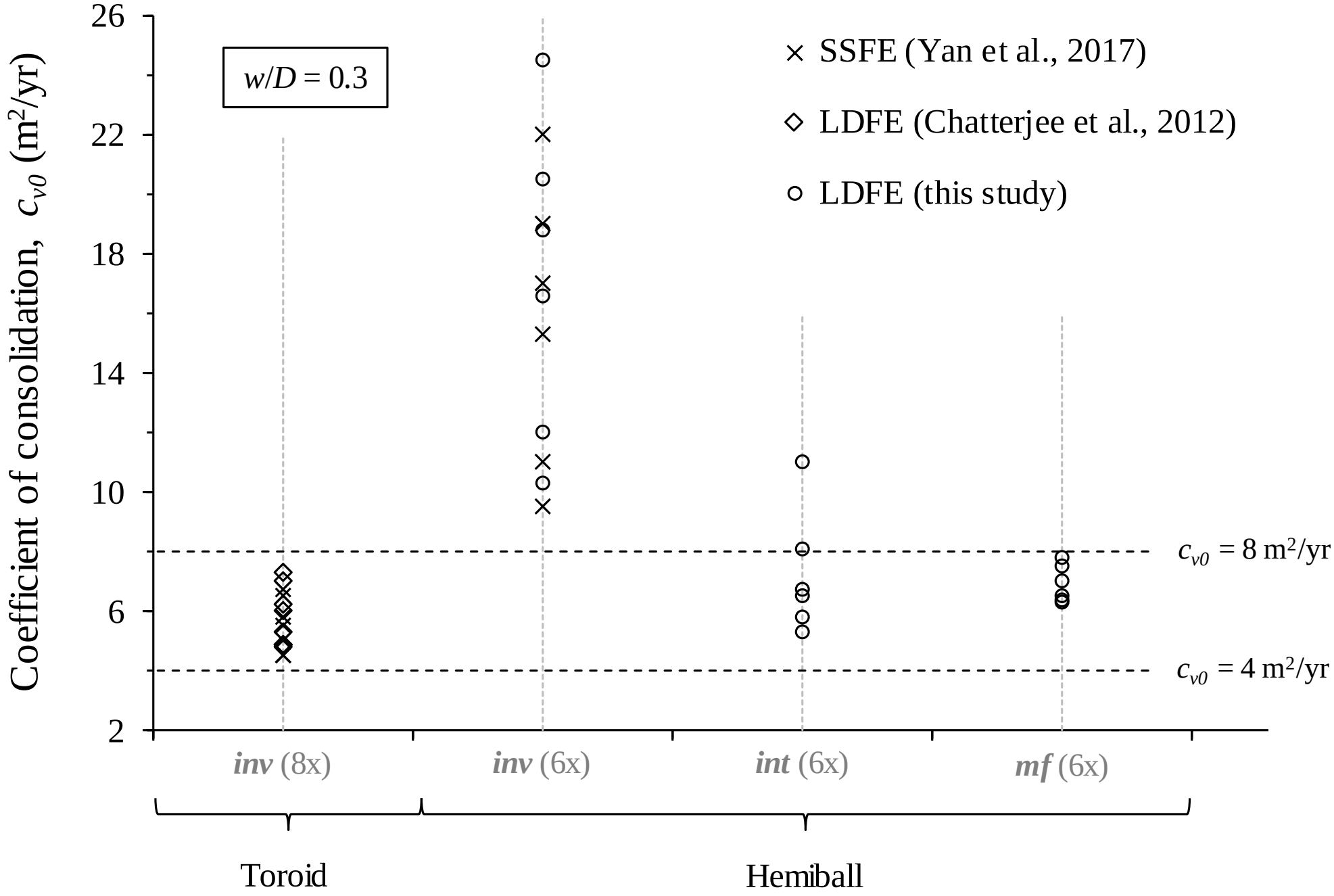
Coefficient of consolidation, c_{v0} (m²/yr)
26
22
18
14
10
6
2
w/D = 0.3
× SSFE (Yan et al., 2017)
◇ LDFE (Chatterjee et al., 2012)
○ LDFE (this study)
c_{v0} = 8 m²/yr
c_{v0} = 4 m²/yr
inv (8x)
inv (6x)
int (6x)
mf (6x)
Toroid
Hemiball

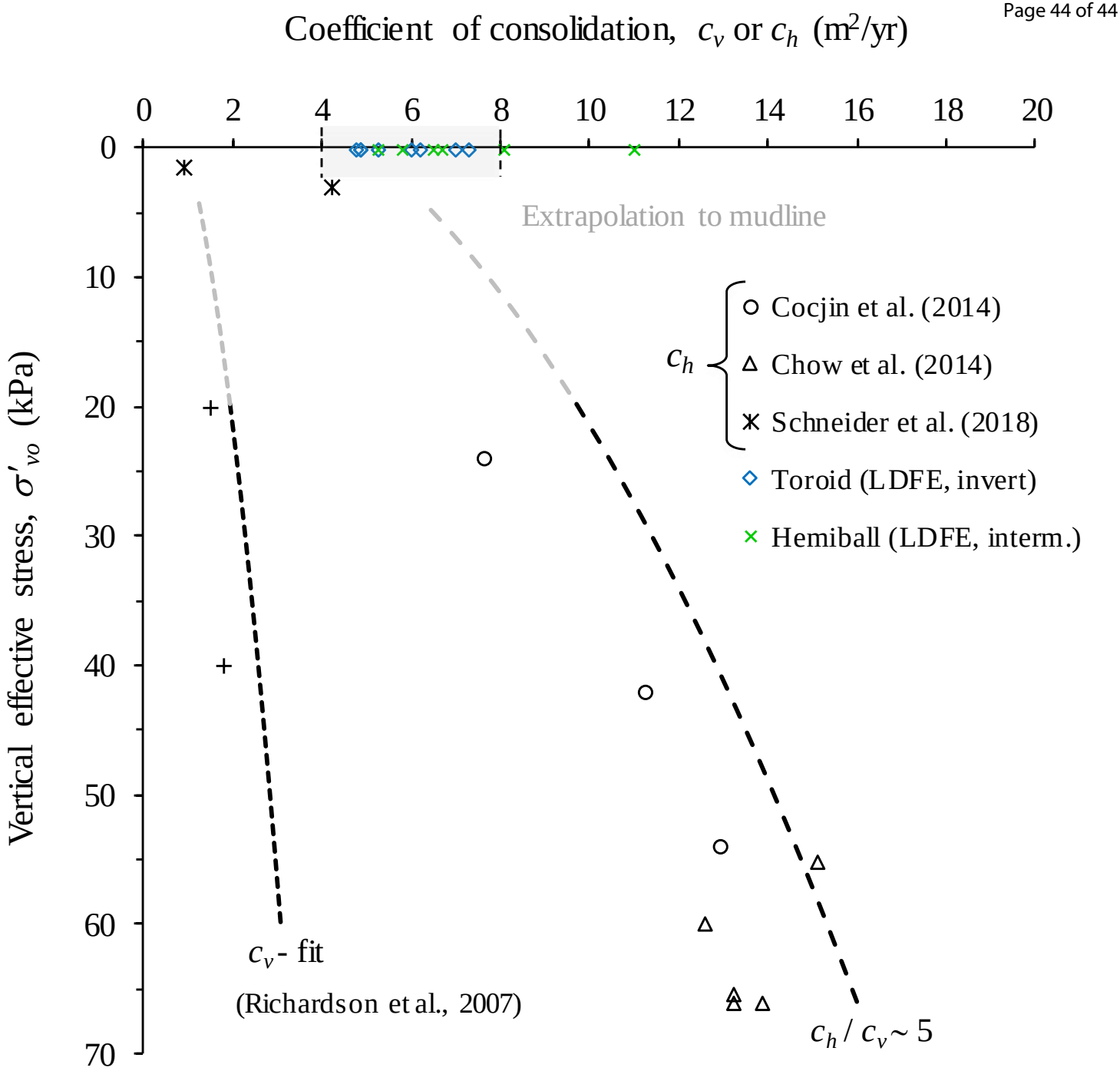
Coefficient of consolidation, c_v or c_h (m²/yr)
0
2
4
6
8
10
12
14
16
18
20
Extrapolation to mudline
Vertical effective stress, σ'_{vo} (kPa)
0
10
20
30
40
50
60
70
c_h
Cocjin et al. (2014)
Chow et al. (2014)
Schneider et al. (2018)
Toroid (LDFE, invert)
Hemiball (LDFE, interm.)
c_v - fit
(Richardson et al., 2007)
c_h / c_v ~ 5